YALE PEABODY MUSEUM

JOURNAL OF MARINE RESEARCH

The *Journal of Marine Research,* one of the oldest journals in American marine science, published important peer-reviewed original research on a broad array of topics in physical, biological, and chemical oceanography vital to the academic oceanographic community in the long and rich tradition of the Sears Foundation for Marine Research at Yale University.

An archive of all issues from 1937 to 2021 (Volume 1–79) are available through EliScholar, a digital platform for scholarly publishing provided by Yale University Library at https://elischolar.library.yale.edu/.

Requests for permission to clear rights for use of this content should be directed to the authors, their estates, or other representatives. The *Journal of Marine Research* has no contact information beyond the affiliations listed in the published articles. We ask that you provide attribution to the *Journal of Marine Research.*

Yale University provides access to these materials for educational and research purposes only. Copyright or other proprietary rights to content contained in this document may be held by individuals or entities other than, or in addition to, Yale University. You are solely responsible for determining the ownership of the copyright, and for obtaining permission for your intended use. Yale University makes no warranty that your distribution, reproduction, or other use of these materials will not infringe the rights of third parties.

The large-scale time-mean ocean circulation in the Nordic Seas and Arctic Ocean estimated from simplified dynamics

by Ole Anders Nøst[1] and Pål Erik Isachsen[1]

ABSTRACT

A simplified diagnostic model of the time-mean, large-scale ocean circulation in the Nordic Seas and Arctic Ocean is presented. Divergences in the surface Ekman layer are extracted from observed climatological wind stress fields. Similarly, divergences caused by the meridional thermal wind transport (relative to the bottom) are calculated from an observed climatological density field. These known quantities are then used to "force" the model's bottom geostrophic velocities.

Both scaling arguments and direct observations show that for long time scales the bottom currents are closely aligned with contours of f/H, (where f is the Coriolis parameter and H is the depth of the seabed). Due to the weak planetary vorticity gradient at high latitudes, the f/H field is dominated by topography and is characterized by multiple regions of closed isolines. The only frictional effect included in the model is bottom stress. By then integrating the depth-integrated vorticity equation over the area spanned by a closed f/H contour, and assuming that the same contour is a streamline of the bottom geostrophic flow, we derive an analytical expression for the bottom geostrophic velocity on this f/H contour. For the few contours that are not closed, current measurements are used as boundary conditions.

Model results are compared with near-bottom current measurements in both the Nordic Seas and the Arctic Ocean. In addition comparison is made with observations from surface drifters in the Nordic Seas by adding the observed thermal wind shear to the modeled bottom flow. The agreement is surprisingly good, suggesting that the simple model is capturing some of the most important processes responsible for the large-scale circulation field. Features like the subgyre recirculations in the Nordic Seas, the gyres in the Canadian and Eurasian Basins, the East Greenland Current, the Norwegian Atlantic Current and the Arctic Circumpolar Boundary Current are all well reproduced by the model. The simplicity of the model makes it well suited as a dynamical framework for interpreting the large-scale circulation pattern in the Nordic Seas and Arctic Ocean.

1. Introduction

One of the more striking features of the large-scale ocean circulation within the Nordic Seas and Arctic Ocean is undoubtedly the way the currents trace out the shape of the underlying ocean basins. As observed and reported nearly a hundred years ago by Helland-Hansen and Nansen (1909), even the surface flow follows the topographic features that form sub-basins, ridges and plateaus hundreds or even thousands of meters below.

1. Norwegian Polar Institute, Polar Environmental Center, 9296, Tromsø, Norway. *email: ole@npolar.no*

More recent studies using surface drifters have given additional evidence (Poulain *et al.*, 1996; Orvik and Niiler, 2002; Jakobsen *et al.*, 2003). This observed behavior tells us that bottom currents in the Nordic Seas and Arctic Ocean must be nonzero. The surface flow would not know about the shape of the ocean basin below if the lower layer were at rest. And indeed, nearly all direct observations from the Nordic Seas and Arctic Ocean show currents near the bottom that are as large as anywhere else in the water column (Aagaard, 1989; Fahrbach *et al.*, 2001; Newton and Sotirin, 1997; Orvik *et al.*, 2001; Woodgate *et al.*, 1999, 2001).

For the Nordic Seas and Arctic Ocean there exist as of yet relatively few dynamical models of low to intermediate complexity, created for the purpose of isolating the lowest-order dynamical balances that govern the large-scale flow. Aagaard (1970), and later Jónsson (1991) and Woodgate *et al.* (1999), have applied flat-bottom Sverdrup dynamics to the Nordic Seas, with a proposed return western boundary current along the East-Greenland continental slope. Their predictions agree with the observed transports in the East Greenland Current (about 30 Sv, see Woodgate *et al.*, 1999), but flat-bottom Sverdrup dynamics is not able to reproduce the circulation patterns seen in the drifter studies mentioned above. Both Jónsson (1991) and Woodgate *et al.* (1999) recognized the neglected effect of topography and suggested that a topographic Sverdrup balance might be more appropriate for the interior regions. In a topographic Sverdrup balance the divergences set up by a wind stress curl are balanced by a net transport perpendicular to isolines of f/H (f being the Coriolis parameter and H the water depth). However, since the f/H field in the Nordic Seas and Arctic Ocean is dominated by the topography, most of these contours close on themselves within the domain north of the Greenland-Scotland Ridge (Fig. 1). In this case of closed f/H contours the topographic Sverdrup balance breaks down; it will violate conservation of mass whenever the net surface forcing within a closed contour is nonzero (Welander, 1968; Hasselmann, 1982).

To our knowledge, the first to consider the dynamical implications of closed f/H contours in the Nordic Seas was Legutke (1991). She found trapping of fluctuations within closed f/H contours to be an important effect in her primitive equation model of the Nordic Seas. Recently, a lowest-order theory for the temporal variability of the recirculating flow within the Nordic Seas and Arctic Ocean has been presented (Isachsen *et al.*, 2003). They looked at the depth-averaged response to temporal anomalies in surface Ekman convergences, assuming that resulting anomalies in depth-integrated transport are aligned with contours of constant f/H. Surface Ekman convergences then spin up gyres contained within regions enclosed by contours of f/H. The spin up continues until finally the divergence in bottom Ekman transport balances the anomalous mass flux convergence of the surface Ekman layer. As such the model results in gyres that spin up cyclonically for cyclonic wind stress anomalies and vice versa. This simple barotropic model turns out to describe sea level fluctuations at monthly to yearly time scales within the Nordic Seas observed by satellite altimetry remarkably well. However, as the time scale increases, one
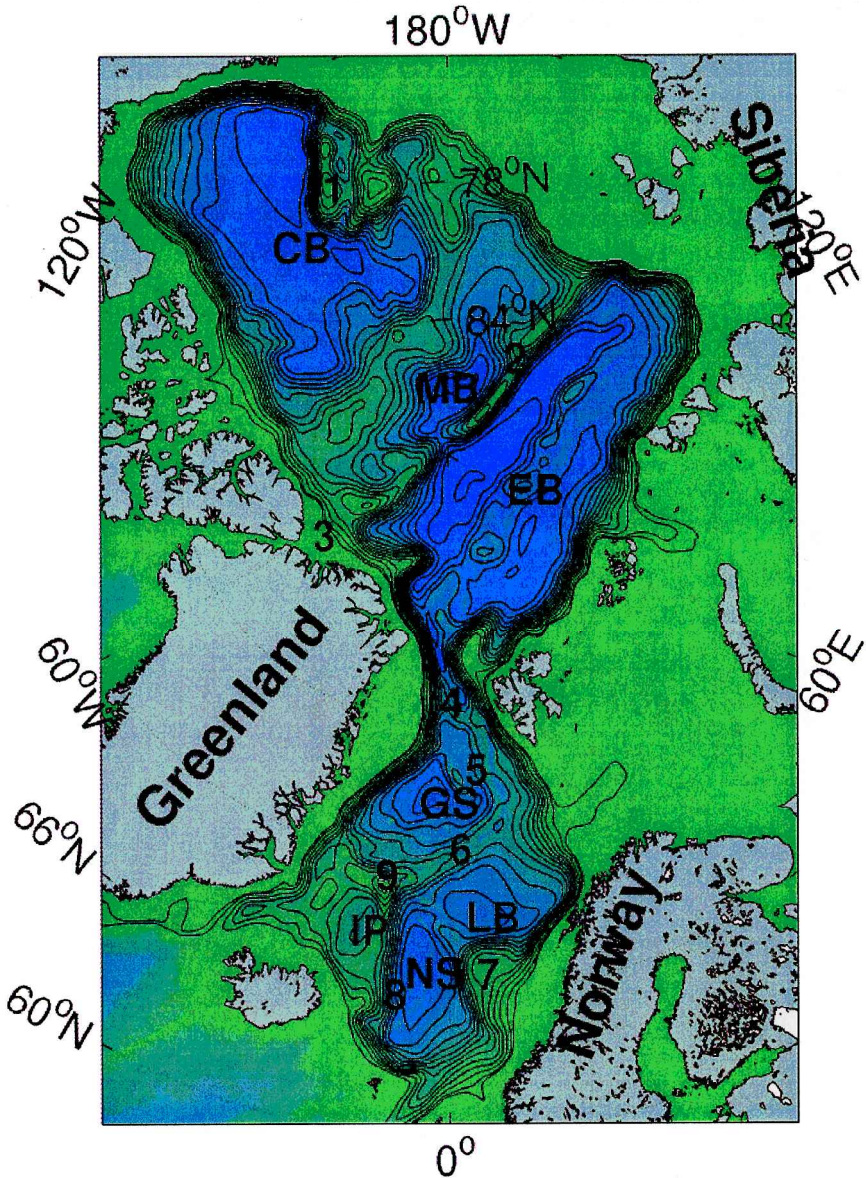
Figure 1. *f/H* contours and seabed topography for the Nordic Seas and Arctic Ocean. The deepest areas (down to about 4000 m) are colored blue while the shallowest areas are colored green. The major basins are marked with their initials. CB—Canada Basin, MB—Makarov Basin, EB—Eurasian Basin, GS—Greenland Sea, LB—Lofoten Basin, NS—Norwegian Sea, IP—Island Plateau. The numbers indicate the location of areas mentioned in the text. 1.—Chuchi Plateau, 2.—Lomonosov Ridge, 3.—Lincoln Sea, 4.—Fram Strait, 5.—Knipovich Ridge, 6.—Mohn Ridge, 7.—Vøring Plateau, 8.—Jan Mayen Ridge, 9.—Jan Mayen.

expects baroclinic pressure fluctuations to eventually gain importance, and a homogeneous model to lose relevance.

The time-mean wind-driven circulation was studied by Welander (1968) in both homogeneous and two-layer oceans. In the homogeneous case, closed f/H contours set up strong gyres. In the two-layer case, the gyres were weak as the surface Ekman pumping was largely balanced by the baroclinic pressure terms. Welander's steady two-layer solution was essentially a Sverdrup balance with a western boundary current in the upper layer. Although interfacial stresses were allowed, the lower layer flow remained weak.

Dewar (1998) also developed an analytical theory for the time-mean circulation in the presence of closed f/H contours. An important element in Dewar's model is an eddy parameterization based on down-gradient diffusion of potential vorticity. In regions of closed f/H contours, this parameterization sets up strong gyres in the lower layers. As such, his model is actually more sensitive to eddy driving than to direct wind forcing, resulting in a gyre circulation whose direction is determined by the topography and not by the sign of the surface forcing. The circulation is cyclonic over topographic lows and anticyclonic over topographic highs. As such, the theory is successful in reproducing the strong anticyclonic circulation over the Zapiola Drift in the South Atlantic, as observed by Saunders and King (1995) and simulated with a primitive equation model by de Miranda *et al.* (1999).

Eddy-topography interaction has also been used as a theoretical explanation for the narrow cyclonic boundary current around the Arctic Ocean. Recent simulations by Nazarenko *et al.* (1998), Nazarenko and Tausnev (2001) and Polyakov (2001) have shown that the parameterization of eddy-topography interaction developed by Holloway (1987, 1992, the "Neptune effect") leads to improved representation of topographically steered boundary currents. Holloway's parameterization acts to drive flow along topography, cyclonic over topographic lows and anticyclonic over topographic highs, similar to that of Dewar (1998). Therefore, gyres driven by the eddy-topography interaction will mainly be cyclonic within the Nordic Seas and Arctic Ocean.

However, the mean wind forcing over much of the Nordic Seas and Arctic Ocean will also tend to set up a cyclonic circulation. The requirement is that a significant part of the surface Ekman pumping is not balanced by divergences in the upper layer but instead transmitted to the bottom layers. Building on these ideas, we will in the next section develop a simple diagnostic model describing the dynamics of the time-mean deep circulation in the Nordic Seas and Arctic Ocean (Section 2). The model is based on potential vorticity budgets within closed contours of f/H. The circulation on the few open f/H contours is determined using available current measurements. The model results are then presented and compared to the circulation picture emerging from available observations (Section 3). Finally, the validity of the model as a lowest-order description of the large-scale time-mean ocean circulation in the Nordic Seas and Arctic Ocean is discussed (Section 4). In general, we conclude that the simple dynamics contained in the model nicely reproduces most features of the large-scale circulation and offers an alternative

explanation for the narrow cyclonic boundary current around the Arctic Ocean and for the deep circulations within the different sub-basins.

2. The model

a. The depth integrated vorticity equation

We start off with the horizontal component of the full equation of motion:

$$\frac{\partial v}{\partial t} + v \cdot \nabla v + k \times fv = -\frac{1}{\rho_0} \nabla p + F \tag{1}$$

where v is the horizontal velocity vector, f is the coriolis parameter, ρ_0 is a reference density, p is pressure (the horizontal gradient operator is used), k is the vertical unit vector and F is a term containing horizontal and vertical frictional stresses. We continue by splitting the horizontal velocity vector into geostrophic and ageostrophic components:

$$v = v_g + v_a, \tag{2}$$

where the geostrophic velocity is given by:

$$v_g = \frac{1}{\rho_0 f} k \times \nabla p. \tag{3}$$

The terms containing accelerations, nonlinearities and friction may now be represented by v_a:

$$k \times fv_a = -\frac{\partial v}{\partial t} - v \cdot \nabla v + F, \tag{4}$$

and the horizontal momentum equation may now be written in the form:

$$k \times fv = -\frac{1}{\rho_0} \nabla p + k \times fv_a. \tag{5}$$

Note that no assumptions or simplifications, other than the Boussinesq approximation, are made at this point.

The depth-integrated transport (per unit horizontal distance) is defined by

$$V = \int_{-H}^{0} v dz, \tag{6}$$

where H is the water depth. The contribution from the sea surface elevation above the zero level has been neglected. Following Bogden *et al.* (1993) we split V into three components:

$$V = V_s + V_a + Hv_b, \tag{7}$$

where V_s is the transport from the integrated geostrophic shear relative to the bottom,

$$V_s = \int_{-H}^{0} (v_g - v_b)dz = \frac{1}{\rho_0 f} k \times \int_{-H}^{0} (\nabla p - \nabla p|_{z=-H})dz, \tag{8}$$

V_a is the depth-integrated transport due to ageostrophic processes,

$$V_a = \int_{-H}^{0} v_a dz, \tag{9}$$

and finally v_b is the bottom geostrophic velocity

$$v_b = \frac{1}{\rho_0 f} k \times \nabla \psi_b = \frac{1}{\rho_0 f} k \times \nabla p|_{z=-H}. \tag{10}$$

Here ψ_b is the streamfunction for $\rho_0 f v_b$.

It can be shown that the divergences of Hv_b and V_s are

$$\nabla \cdot (Hv_b) = -\frac{H^2}{f} v_b \cdot \nabla \frac{f}{H}, \tag{11}$$

$$\nabla \cdot V_s = -V_s \cdot \frac{\nabla f}{f}. \tag{12}$$

We now average over sufficiently long time scales, which implies zero transport divergence. Using (7), (11), (12) and setting $\nabla \cdot V = 0$, we arrive at a useful form of the depth-integrated vorticity equation:

$$\frac{H^2}{f} v_b \cdot \nabla \frac{f}{H} = -V_s \cdot \frac{\nabla f}{f} + \nabla \cdot V_a \tag{13}$$

By the geostrophic relation (10) and repeated use of Gauss' theorem, it can be shown that the left hand side of (13) will vanish when integrated over the area A enclosed by an f/H contour. The resulting integral expression is

$$\iint_A \left(-V_s \cdot \frac{\nabla f}{f} + \nabla \cdot V_a \right) dA = 0. \tag{14}$$

Thus, integrated over the area enclosed by an f/H contour, the divergence of the total ageostrophic transport must be balanced by the divergence caused by a meridional thermal wind transport (relative to the bottom flow). Note that near the geographic north pole a vanishingly small planetary vorticity gradient requires that the ageostrophic transport out of the enclosed region (by Gauss' theorem) more or less balance.

Although illustrative, (14) is only an integral balance. To solve for the flow everywhere we either need more information or we must make assumptions about the bottom

geostrophic velocity, the thermal wind shear and the ageostrophic transport. To proceed, we will consider the thermal wind transport as a known quantity (estimated from hydrographic data) and make assumptions about the geostrophic bottom velocity and about the processes responsible for the ageostrophic transports.

b. Scalings and simplifications

We consider the time-mean flow in which the only ageostrophic transports are within the surface and bottom Ekman layers. In addition to keeping the model simple, it is quite conceivable that the bottom Ekman layer plays an important role considering the large bottom flows observed. The divergence of the ageostrophic transport becomes:

$$\nabla \cdot V_a = \nabla \times \frac{\tau_s}{\rho_0 f} - \nabla \times \frac{\tau_b}{\rho_0 f}, \tag{15}$$

where τ_s is the stress at the surface and τ_b is the stress at the bottom. With these assumptions, the depth-integrated vorticity equation (13) now takes the form

$$\frac{H^2}{f} v_b \cdot \nabla \frac{f}{H} + \nabla \times \frac{\tau_b}{\rho_0 f} = \nabla \times \frac{\tau_s}{\rho_0 f} - V_s \cdot \frac{\nabla f}{f}. \tag{16}$$

The "unknown" terms consisting of the divergence of Hv_b and the divergence in the bottom Ekman layer are placed on the left-hand side. The right-hand side consists of quantities extracted from data, and we will repeatedly be calling these the "forcing" terms for the bottom flow. They consist of the divergences set up by the surface Ekman layer and the meridional component of the thermal wind transport relative to the bottom.

It is these two forcing terms that would mutually cancel in a Sverdrup balance with no motion in the lower layers. Estimates of their sizes in the Nordic Seas and Arctic Ocean are shown in Figure 2. The divergence of the surface Ekman layer (Fig. 2a) was calculated using wind stress data from the NCEP/NCAR reanalysis project (Kalnay *et al.,* 1996) averaged over the period from 1950–2000. The divergence of the meridional component of the thermal wind transport relative to the bottom (Fig. 2b) was derived by merging seasonal average hydrographic fields from the EWG Arctic Atlas (Timokhov and Tanis, 1997, 1998) (north of 65N) and the World Ocean Atlas 1998 (Conkright *et al.,* 1998) (south of 65N). These two terms have quite different spatial distributions and in general do not cancel (Fig. 3). A pure Sverdrup balance therefore does not seem to have any relevance to the dynamics in the Nordic Seas and Arctic Ocean. Nonzero bottom velocities and, in the context of this particular model, bottom frictional layers are required.

Expecting nonzero bottom flows, the area-integrated balance (14) may now be written (applying Stoke's theorem to the bottom Ekman transport):
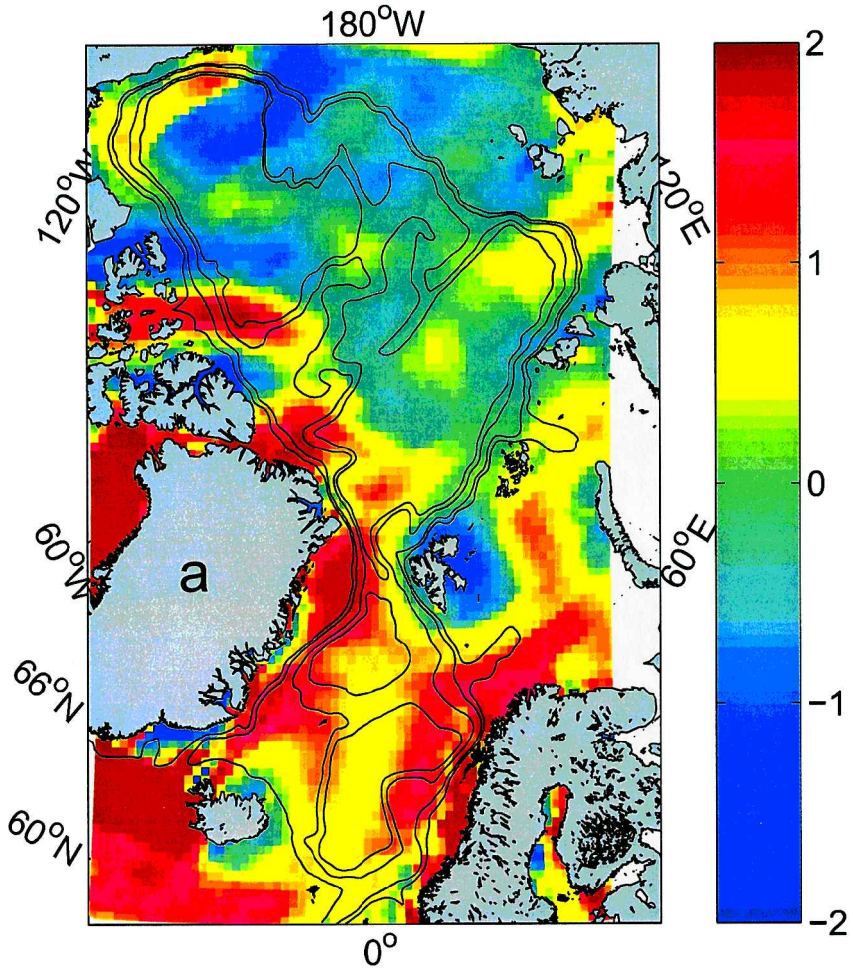
Figure 2. (a) Ekman pumping velocities given by $\nabla \times \boldsymbol{\tau}_s / \rho_0 f$ calculated from NCEP wind stress data
and (b) hydrographic forcing given by $-\boldsymbol{V}_s \cdot \nabla f / f$ calculated from EWG Arctic Atlas and World
Ocean Atlas 98. The units are 10^{-6} m s^{-1}

$$\oint_C \frac{\boldsymbol{\tau}_b}{\rho_0 f} \cdot \boldsymbol{t} dl = \int\int_A \left(\nabla \times \frac{\boldsymbol{\tau}_s}{\rho_0 f} - \boldsymbol{V}_s \cdot \frac{\nabla f}{f} \right) dA, \tag{17}$$

where C is the f/H contour enclosing the area A, and $\boldsymbol{t}$ is the tangent unity vector to C in a
counter-clockwise direction.

To represent the bottom stress we use a quadratic bottom friction law

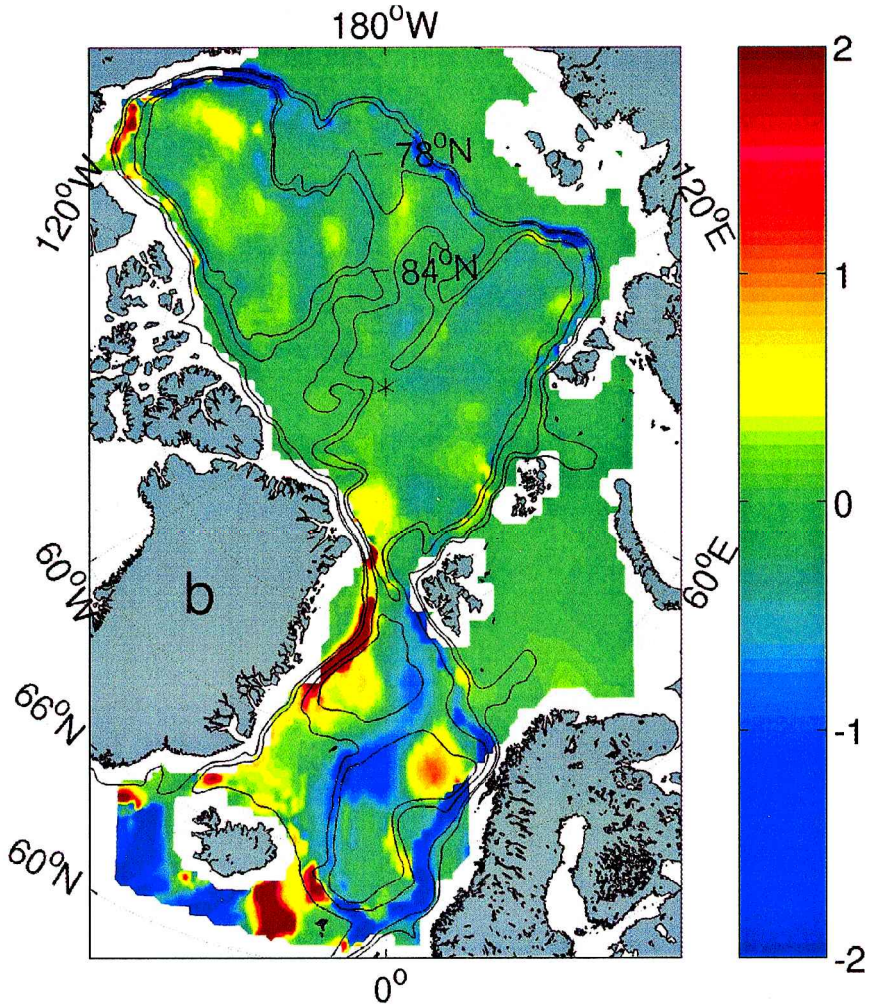$$\boldsymbol{\tau}_b = \rho_0 C_D \sqrt{u_b^2 + v_b^2} \, \boldsymbol{v}_b, \tag{18}$$

Figure 2. (Continued)

where C_D is a drag coefficient, with typical values of order 10^{-3} (Haidvogel and Beckmann, 1999). Alternatively we may also use a linear friction law:

$$\boldsymbol{\tau}_b = \rho_0 R \boldsymbol{v}_b, \tag{19}$$

where values of the linear friction parameter R should be of order 10^{-4} m s^{-1} (Haidvogel and Beckmann, 1999).

To proceed, we start by finding representative scales for the bottom geostrophic velocities. The forcing field shown in Figure 3 may be looked upon as the part of the surface forcing which is not balanced by baroclinic terms, and we assume that this part is
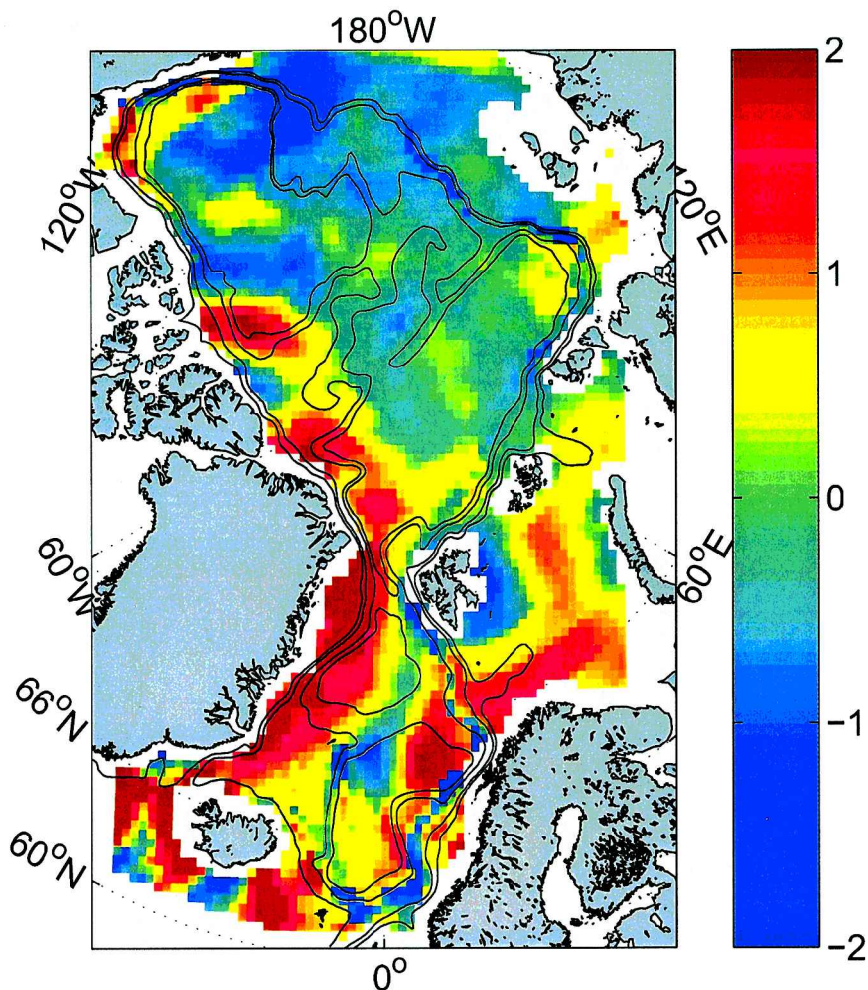
Figure 3. The sum of Ekman pumping (Fig. 2a) and hydrographic forcing (Fig. 2b) given by the right hand side of (16). The units are 10^{-6} m s^{-1}.

directly forcing the deep circulation. The area-integrated budget (17) tells us that, within the areas enclosed by each closed f/H contour, the mean bottom Ekman pumping equals the mean forcing. Therefore, we make the assumption that the divergence of the bottom Ekman layer is the same order of magnitude as the forcing.

From Figure 3, we see that vertical velocities associated with the forcing are of order 10^{-6} m s^{-1}. From this we can now estimate an approximate scale for the bottom geostrophic velocity. The topographically steered currents have transverse length scales approximately equal to the widths of continental slopes and ridges, typically a few hundred kilometers. Assuming a transverse length scale L of order 10^5 m, Coriolis parameter f of

order $10^{-4}\,\mathrm{s}^{-1}$ and drag coefficient C_D of order 10^{-3}, we get (using a quadratic bottom friction law)

$$\nabla \times \frac{\boldsymbol{\tau}_b}{\rho_0 f} = \nabla \times \frac{C_D(v_b)^2}{f} \approx \frac{C_D U^2}{fL} \approx 10^{-6}\,\mathrm{ms}^{-1}$$

$$\Downarrow \tag{20}$$

$$U \approx 10^{-1}\,\mathrm{m\ s}^{-1}.$$

Bottom velocities of these magnitudes are frequently observed (Newton and Sotirin, 1997; Woodgate *et al.,* 1999; Fahrbach *et al.,* 2001; Orvik *et al.,* 2001; Woodgate *et al.,* 2001), and we take this as a first indication that a model using bottom friction may give reasonable results.

The term in the depth-integrated vorticity equation (16) involving the flow perpendicular to the f/H contours has to be of the same order of magnitude or smaller than the other terms. We will assume that it is of the same order of magnitude as the divergence in the bottom Ekman layer, and we may then estimate the scale of the bottom velocity perpendicular to the f/H contours. As can be seen in Figure 4, most of the Nordic Seas and Arctic Ocean, except for the basin centers and shelf areas, have topographic gradients of order 10^{-3} or larger. Using 10^{-3} as a typical value for the topographic slope, together with the fact that the gradient of the f/H field in these ocean regions is dominated by the topographic effect, we get

$$\frac{H^2}{f}\,\boldsymbol{v}_b \cdot \nabla \frac{f}{H} \approx -U_\perp |\nabla H| \approx \frac{C_D U^2}{fL} \approx 10^{-6}\,\mathrm{m\ s}^{-1}$$

$$\Downarrow \tag{21}$$

$$\frac{U_\perp}{U} \approx \frac{C_D U}{fL|\nabla H|} \approx 10^{-2},$$

where $U_\perp$ is a scale for the geostrophic velocity perpendicular to the f/H contours. In slope regions where topographic gradients are typically larger than 10^{-3} the ratio between the total velocity and the component perpendicular to the f/H contours are probably smaller than the above estimate. The bottom geostrophic velocity is therefore directed nearly parallel to the f/H contours.

It is practical to introduce a new coordinate, $q = f/H$ and another coordinate, s, which has isolines everywhere perpendicular to those of q. In terms of q and s the bottom geostrophic velocity (10) may be written:

$$\boldsymbol{v}_b = \frac{1}{\rho_0 f}\frac{\partial \psi_b}{\partial q}\boldsymbol{k} \times \nabla q + \frac{1}{\rho_0 f}\frac{\partial \psi_b}{\partial s}\boldsymbol{k} \times \nabla s, \tag{22}$$
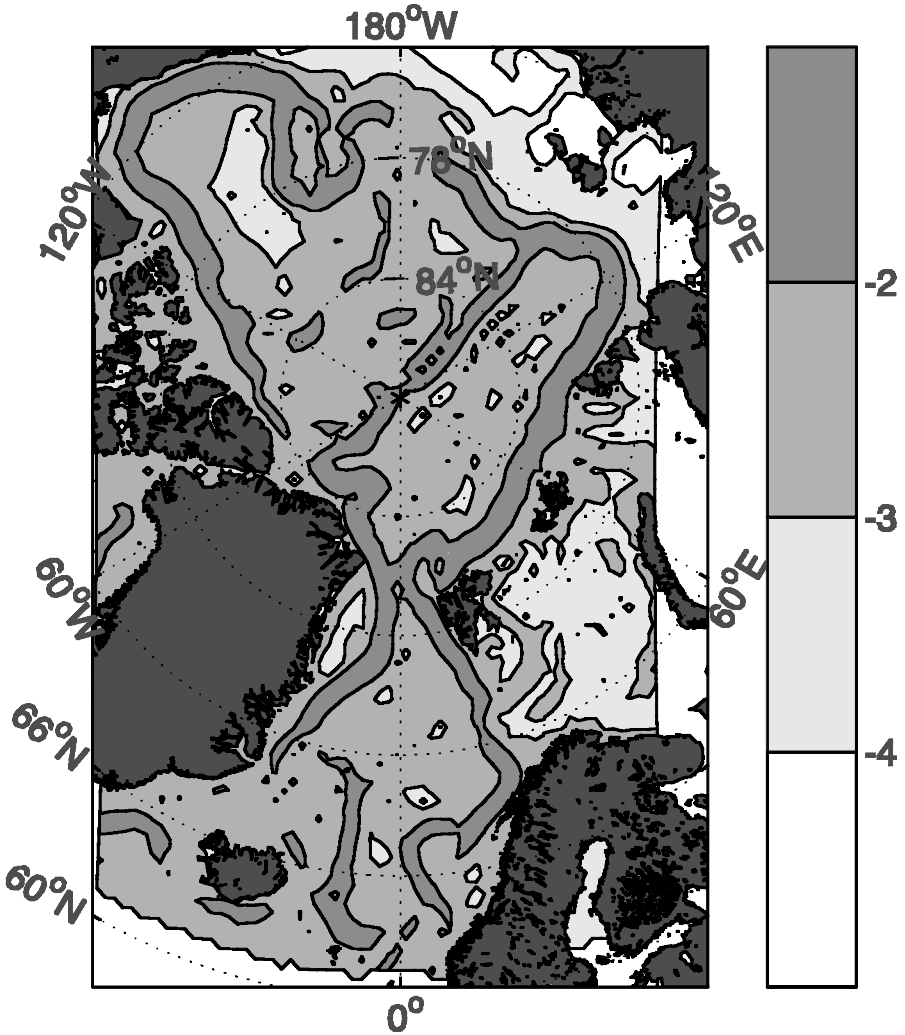
Figure 4. The topographic gradient (log 10 logarithmic scale) as calculated from the TerrainBase
$(5' \times 5')$ dataset.

i.e., in terms of the geostrophic velocity components parallel (with scale $U_\parallel$) and
perpendicular (with scale $U_\perp$) to the q contours. Since $U_\parallel$ is much larger than $U_\perp$ we may
represent the bottom velocity with $U_\parallel$ only:

$$\boldsymbol{v}_b \cong \frac{1}{\rho_0 f} \frac{\partial \psi_b}{\partial q} \boldsymbol{k} \times \nabla q. \tag{23}$$

The problem is now reduced to finding $\partial \psi_b / \partial q$, which is related to the transport between
two neighboring q contours.

The simplest way to proceed is to assume that ψ_b (and hence $\partial\psi_b/\partial q$) is a function of q only, being equivalent to assuming that contours of ψ_b and contours of q are parallel. This assumptions has been frequently used by other investigators in the case of closed contours of potential vorticity (Rhines and Young, 1982; Dewar, 1998; Isachsen *et al.,* 2003). Additional scaling arguments (see Appendix A) suggest that the assumption is a reasonable one, also in our region of interest, and we proceed to the simple final expressions it allows us to form.

c. Estimating bottom velocities on closed f/H contours

Inserting the approximate expression for the bottom geostrophic velocity (23) into the quadratic bottom friction (18) gives:

$$\boldsymbol{\tau}_b = \rho_0 C_D |\boldsymbol{v}_b| \boldsymbol{v}_b = \frac{C_D}{\rho_0 f^2} \left|\frac{\partial\psi_b}{\partial q}\right| \frac{\partial\psi_b}{\partial q} \left|\nabla q\right| \boldsymbol{k} \times \nabla q. \tag{24}$$

Substitution of this into the area-integrated potential vorticity balance (17), treating $\partial\psi_b/\partial q$ as constant for any given f/H contour enables us to solve for $\partial\psi_b/\partial q$:

$$\left|\frac{\partial\psi_b}{\partial q}\right| \frac{\partial\psi_b}{\partial q} = \frac{\rho_0^2}{C_D} \frac{\displaystyle\iint_A \left(\nabla \times \frac{\boldsymbol{\tau}_s}{\rho_0 f} - \boldsymbol{V}_s \cdot \frac{\nabla f}{f}\right) dA}{\displaystyle\oint_C \frac{|\nabla q|}{f^3} (\boldsymbol{k} \times \nabla q) \cdot \boldsymbol{t}\, dl}. \tag{25}$$

Finally, back-substitution into (24) gives us the bottom velocity:

$$|\boldsymbol{v}_b| = \frac{1}{f} \left(\left|\iint_A \left(\nabla \times \frac{\boldsymbol{\tau}_s}{\rho_0 f} - \boldsymbol{V}_s \cdot \frac{\nabla f}{f}\right) dA\right| \frac{|\nabla q|^2}{C_D \displaystyle\oint_C \frac{|\nabla q|^2}{f^3} dl}\right)^{1/2}, \tag{26}$$

where the direction is given by the sign of the area-integral. By repeating the same procedure using the linear friction law (19) we would end up with:

$$\frac{\partial\psi_b}{\partial q} = \frac{\rho_0}{R} \frac{\displaystyle\iint_A \left(\nabla \times \frac{\boldsymbol{\tau}_s}{\rho_0 f} - \boldsymbol{V}_s \cdot \frac{\nabla f}{f}\right) dA}{\displaystyle\oint_C \frac{(\boldsymbol{k} \times \nabla q) \cdot \boldsymbol{t}}{f^2} dl}, \tag{27}$$

and

$$v_b = \frac{1}{Rf} \iint_A \left(\nabla \times \frac{\boldsymbol{\tau}_s}{\rho_0 f} - \boldsymbol{V}_s \cdot \frac{\nabla f}{f} \right) dA \; \frac{|\nabla q|}{\oint_C \frac{|\nabla q|}{f^2} dl} \boldsymbol{t}. \tag{28}$$

The derivations using linear and quadratic friction gives qualitatively the same results. The average bottom velocity around an f/H contour is controlled by the area-integral of the forcing, while the distribution of the velocity around a contour is given by the local gradient divided by the mean gradient of f/H. The sense of circulation around a contour is always given by the sign of the area-integrated forcing.

To illustrate the essentials of the dynamics we consider an asymmetrically shaped gyre forced with an Ekman pumping velocity which is constant in space and equal to 10^{-6} m s^{-1}. The resulting bottom geostrophic velocities, estimated from (28), are shown in Figure 5a. The role of the bottom Ekman layer is to balance the potential vorticity budget within a closed f/H contour, in an *averaged* sense. Therefore, the average bottom Ekman pumping within each contour will equal the constant forcing. However, the bottom Ekman layer is incapable of achieving a point-wise balance because the bottom geostrophic velocity is forced to vary according to the gradient of the f/H field. In Figure 5b we clearly see that the strongest bottom Ekman pumping is found in the area with strongest gradients of the f/H field. To achieve a *point-wise* balance of the potential vorticity budget, vertical velocities resulting from bottom geostrophic velocities perpendicular to the f/H contours will be needed. This term is calculated from (16), where it balances out the difference between the forcing and the bottom Ekman pumping, and is shown in Figure 5c. In the area with large positive bottom Ekman pumping the "cross-f/H term" is negative, as the bottom Ekman pumping is larger than the forcing, leading to geostrophic velocities towards increasing depth. In the areas with weak bottom Ekman pumping the geostrophic velocities will be towards decreasing depth. However, as shown by the preceding scaling arguments, the geostrophic velocity component perpendicular to the f/H contours that is creating the vertical velocities shown in Figure 5c is much smaller than the velocity parallel to the f/H contours. Therefore, (26) and (28) give good estimates of the total velocity. Another example of flow in an idealized basin where an analytical solution based on (28) is compared to a numerical solution of (16) is presented in Appendix B.

d. Estimating bottom velocities on open f/H contours

From (23), it is clear that if we know $\partial \psi_b / \partial q$ at any point on an f/H contour, we will know the bottom flow everywhere on that same contour. However, on open contours we cannot use the integral constraint given by (17). For the Nordic Seas and Arctic Ocean, the upper parts of the continental slope consist of contours that cross the Greenland-Scotland
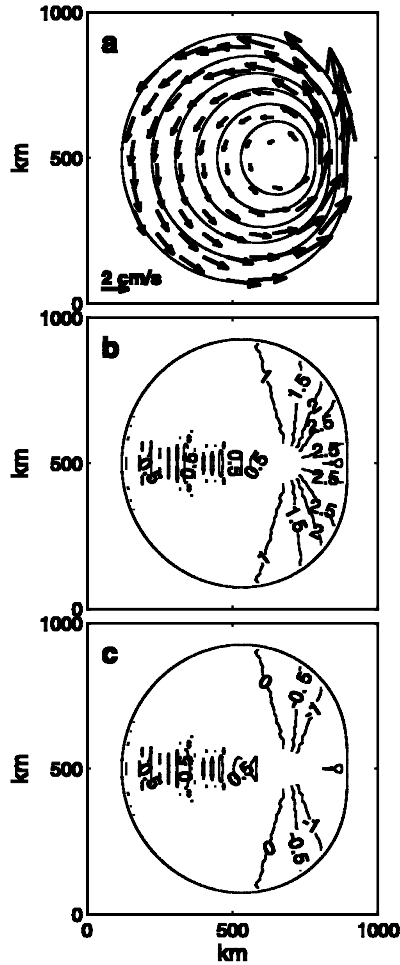
Figure 5. The circulation given by (28) in an idealized gyre. The forcing is constant in space and equal to 10^{-6} m s^{-1}. (a) The f/H contours and bottom geostrophic velocities. (b) The bottom Ekman pumping term calculated from the curl of the bottom geostrophic velocity. (c) The vertical velocities resulting from a geostrophic velocity component perpendicular to the f/H contours, calculated from (16) when forcing and bottom Ekman pumping is known. In (b) and (c) the units of the contour labels are 10^{-6} m s^{-1}.

Ridge into the North Atlantic. We treat these as open contours and, to avoid having to deal with dynamics at lower latitudes, we will instead estimate the value of $\partial\psi_b/\partial q$ from direct observations. We assume that $\partial\psi_b/\partial q$ may be treated as a function of q also on the open f/H contours. As the bottom currents observed on these contours often exceed 0.1 m s^{-1} (Aagaard, 1989; Fahrbach *et al.,* 2001; Newton and Sotirin, 1997; Orvik *et al.,* 2001), and
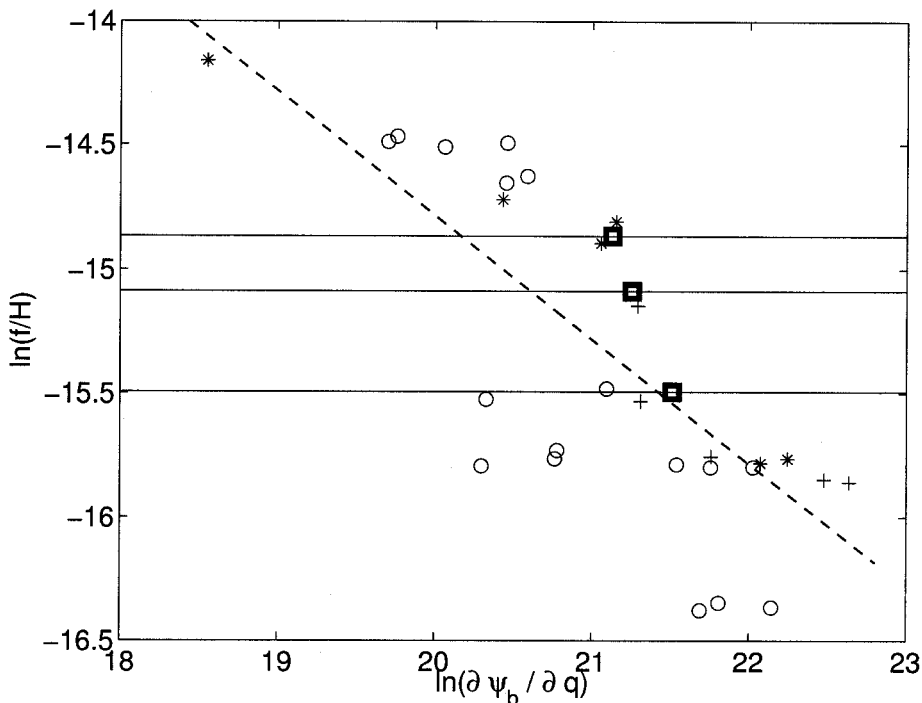
Figure 6. A log-log plot of f/H versus $\partial\psi_b/\partial q$, where $\partial\psi_b/\partial q$ is calculated for the open f/H contours using current meter observations from Fram Strait ($\bigcirc$) (Fahrbach *et al.,* 2001), from 75N in the Greenland Sea ($*$) (Woodgate *et al.,* 1999) and from the Svinøy section ($+$) (Orvik *et al.,* 2001).

the topographic slope along these contours is larger than 10^{-2}, this should be a reasonable assumption.

We use direct current measurements from the Norwegian continental slope (Orvik *et al.,* 2001), from the Fram Strait (Fahrbach *et al.,* 2001), and from the Greenland continental slope (Woodgate *et al.,* 1999), together with bathymetric data, to estimate the value of $\partial\psi_b/\partial q$ on three open contours. The estimate is based on the approximate expression for the bottom geostrophic velocity (23), where all the terms except $\partial\psi_b/\partial q$ are estimated from the data. The data and resulting estimates are shown in Figure 6.

Note that when the f/H gradient is dominated by topography, the magnitude of $\partial\psi_b/\partial q$ is approximately given by:

$$\left|\frac{\partial\psi_b}{\partial q}\right| = \frac{\rho_0 f\,|\boldsymbol{v}|}{|\nabla q|} \approx \frac{\rho_0 f^2|\boldsymbol{v}|}{|\nabla H|}\left(\frac{f}{H}\right)^{-2}. \tag{29}$$

Roughly then, a log-log plot of $\partial\psi_b/\partial q$ vs. f/H should scatter the data around a straight line with slope -0.5. Such a line has been added to Figure 6 and generally confirms this relationship.

This method of obtaining bottom velocities everywhere on open f/H contours probably has large uncertainties. However, it is the best way of initializing the flow on the open contours that we can think of and, as shown below, the flow field predicted by the model on other segments of the same contours is quite close to that observed.

3. Model results and comparison with observations

To estimate the large-scale bottom flow of the Nordic Seas and Arctic Ocean with this simplified model, we need a set of f/H contours, a surface wind stress field and a density field for the Nordic Seas and Arctic Ocean. The f/H field (Fig. 1) was generated with bathymetry extracted from the TerrainBase ($5' \times 5'$) topographic data set (National Geophysical Data Center, 1995). As we are interested in large-scale circulation features, smoothing was applied to remove scales smaller than roughly 30 km. As mentioned in the above, surface stresses were extracted from NCEP/NCAR Reanalysis and hydrography from a combination of the EWG Arctic Atlas and the World Ocean Atlas 98. Finally the drag coefficient C_D for a quadratic bottom friction law was set equal to 10^{-3}.

Bottom geostrophic velocities were calculated from (26) for closed contours, and by (23) and (29) for open contours. These calculations were made for a number of points on each of these contours and finally interpolated onto a regular grid for presentation (Fig. 7). The large-scale bottom flow is characterized by the narrow Arctic Circumpolar Boundary Current (ACBC; Aagaard, 1989; Rudels *et al.,* 1999) flowing counter-clockwise along the perimeter of the entire domain, and by smaller gyres associated with the different sub-basins of the Nordic Seas and Arctic Ocean. This first impression is encouraging, and we move on to a closer look at details, first in the Nordic Seas and then in the Arctic Ocean.

a. Nordic Seas

Figure 8 shows the modeled bottom currents in the Nordic Seas together with direct observations of near-bottom currents at several locations. The fit is generally good, but notable exceptions exist.

At the continental slope north of the Faeroe Islands the magnitudes of the modeled currents are in good agreement with an observation from that region. But the directions do not agree very well. A closeup of this region (Fig. 9) leads us to speculate that finer details of the local topography is to blame. The local isobaths at the mooring, at the resolution of the original topographic dataset, are directed north–south, and the observed current is aligned in this direction. In contrast, the modeled currents follow the smoothed isobaths. This is but one example of a difficulty we will repeatedly encounter in comparing point measurements with predictions from a theory meant to represent spatially averaged currents. Eularian current measurements are suitable for forming rigorous temporal statistics but typically suffer from an extreme spatial undersampling.

In the Svinøy section which crosses the Norwegian continental slope, the model generally does well, but underestimates the strongest currents near the coast by more than a
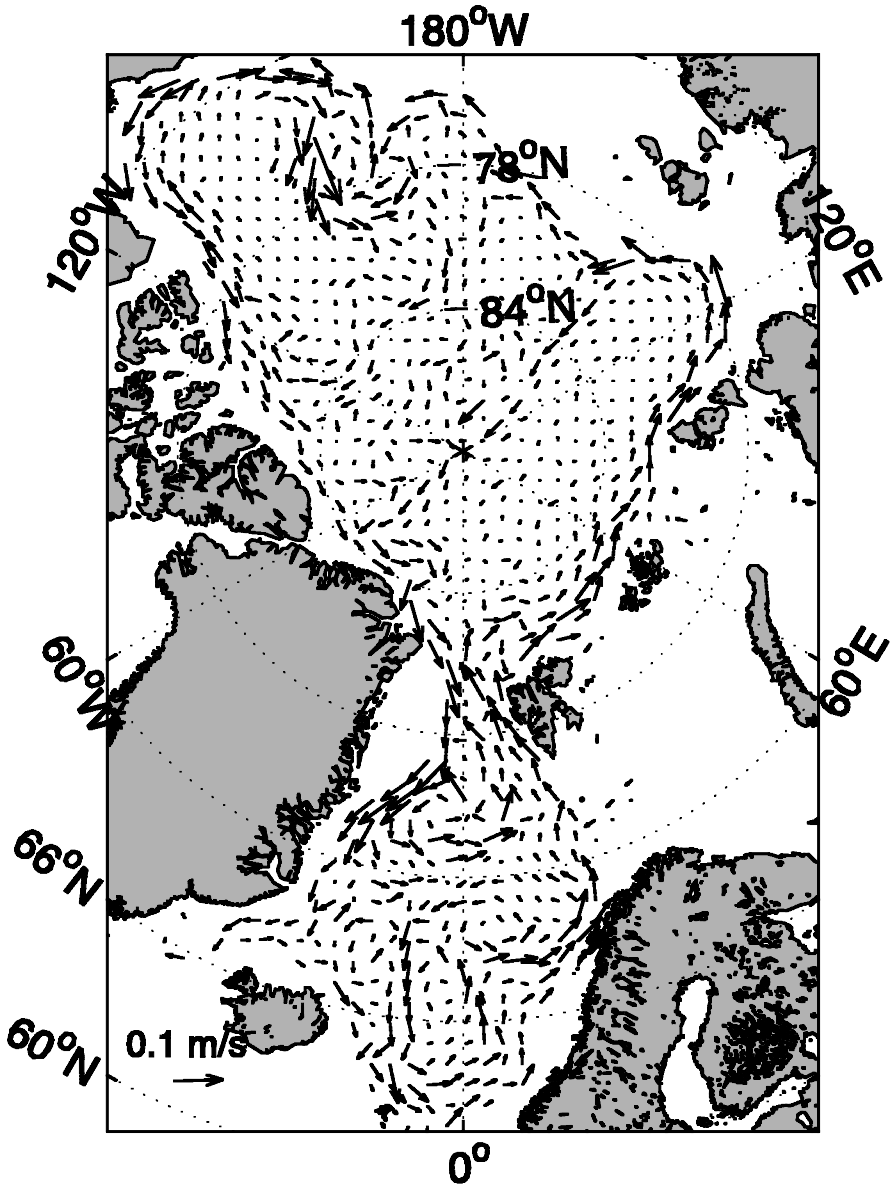
Figure 7. Modeled bottom geostrophic velocities in the Nordic Seas and Arctic Ocean.

factor of two. The reported direction of near-bottom currents at one location, near the 1000 m isobath, is also radically different from the model predictions. Farther north, two isolated observations from the slope of the Vøring Plateau each agree well with modeled currents.
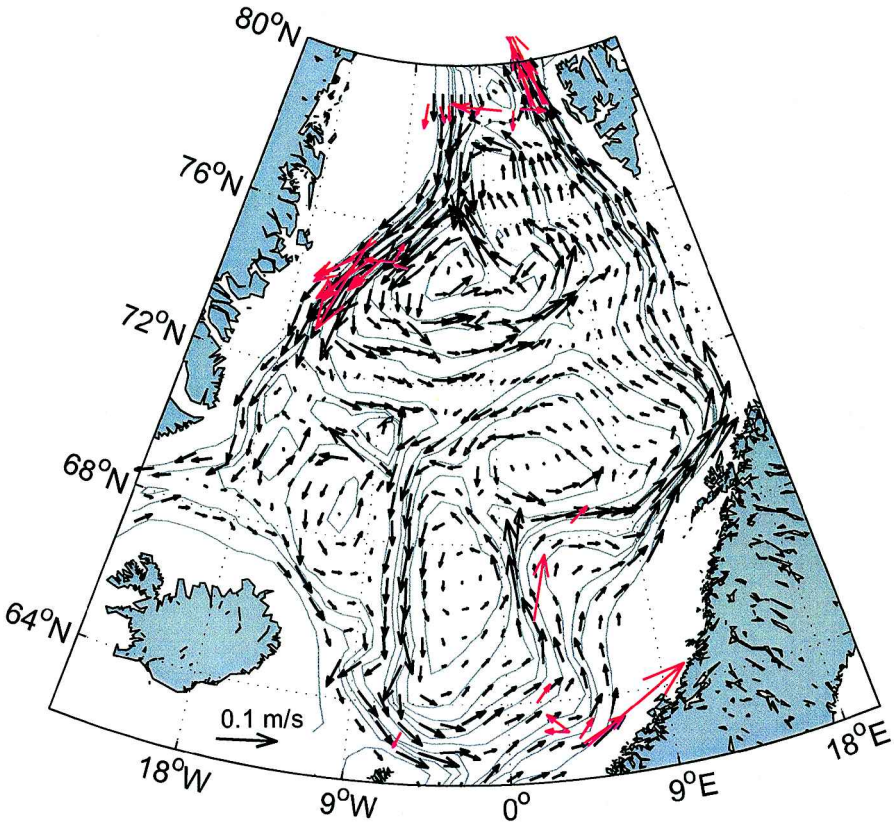
Figure 8. Modeled bottom geostrophic velocities (black arrows) and observed near-bottom currents (red arrows) for the Nordic Seas. The sources of the observed near-bottom currents are from S. Østerhus (pers com.) (the slope of the Vøring Plateau and on the slope north of the Faeroe Islands), Orvik *et al.* (2001) (Svinøy section near the coast of Norway), Woodgate *et al.* (1999) (Greenland Sea), and Fahrbach *et al.* (2001) (Fram Strait).

In the Fram Strait there is more data to work with. On both eastern and western flanks the agreement is quite good, except perhaps for a slight tendency by the model to underesti-mate the magnitudes in the east while overestimating them in the west. In the central areas of the Fram Strait the agreement again appears more random. This may very well in part be due to local fine-scale topographic effects. Finally, along the Greenland continental slope near 75N the agreement appears to be good.

The use of Lagrangian surface drifters in the Nordic Seas has resulted in surface flow field estimates that we can use with some statistical confidence. Early results were presented by Poulain *et al.* (1996) and recently Jakobsen *et al.* (2003) have improved these estimates by adding additional years of observations. The most recent dataset is based on 114 individual satellite tracked drifters in the time period from June 1991 to May 1995.
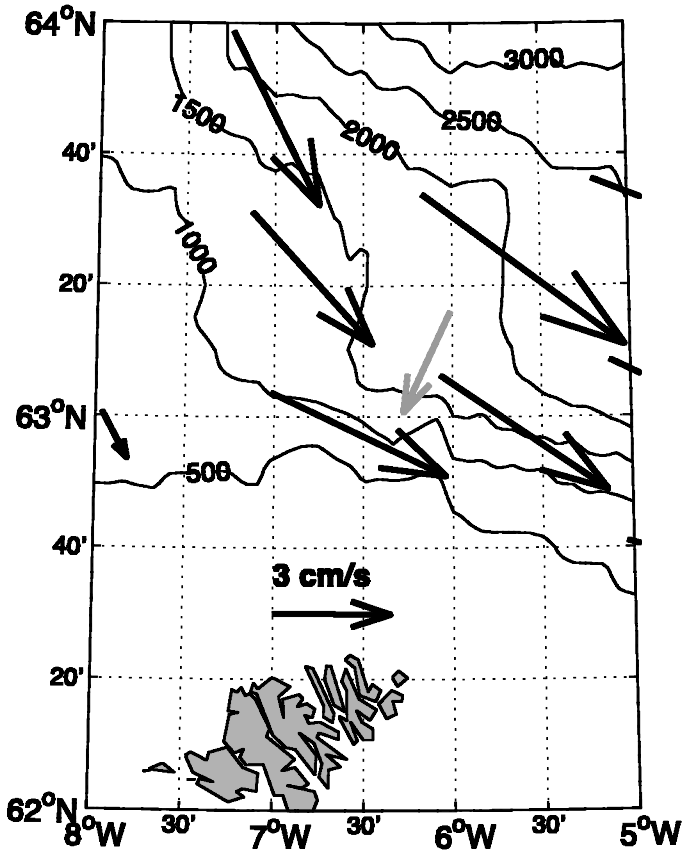
Figure 9. The effect of local topography. A blow up of the area around the current meter measurements on the slope north of the Faeroe Islands. The modeled currents (black arrows) follow the smoothed f/H field (not shown), while the observed current (gray arrow) follow the non-smoothed topographic contours which is shown in the figure.

The southern and eastern parts of the Nordic Seas were well covered with drifters, while in the northern and western parts the coverage was more sparse. We thus attach higher confidence to their estimates for the southern and eastern parts than to those for the northern and western parts. The time-mean surface field, as reported by Jakobsen *et al.,* is shown in Figure 10.

The present model gives an estimate for the bottom geostrophic flow. To compare with observed surface currents we add the observed thermal wind shear from the bottom to the surface. Note that this shear (as recorded in the hydrography) may also be interpreted as a solution to the depth-integrated vorticity equation in the case of complete "compensation" at depth such that lower layers are at rest (zero left hand side in 16). To see if the model represents an improvement from this other theoretically possible solution, Figure 11 shows
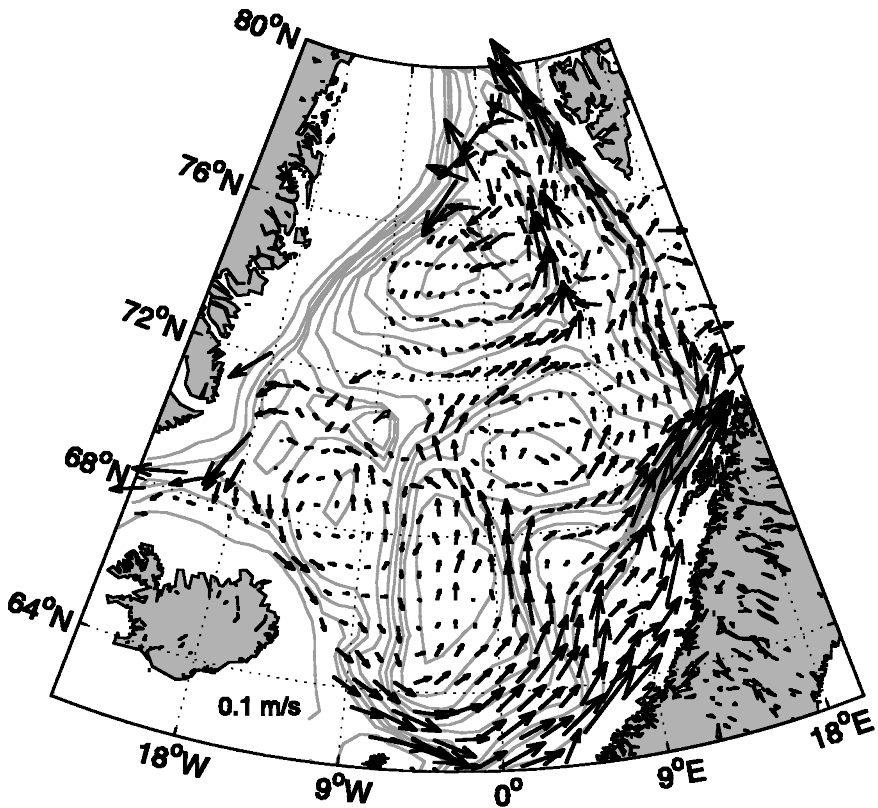
Figure 10. Mean surface flow in the Nordic Seas from Lagrangian drifters (Jakobsen *et al.,* 2003).

both the thermal wind shear alone in (a) and the sum with the modeled bottom currents in (b). The first impression is that the model does a very good job in describing the main features of the surface circulation in the Nordic Seas. Much of the information about surface currents is certainly contained in the density field, e.g. the cyclonic gyration in the Greenland Sea and around the Island Plateau as well as the re-circulation in the northern parts of the Fram Strait. However, closer comparison with the observed currents (Fig. 10) reveals a number of features in the surface circulation that do require nonzero bottom flows.

The surface currents on the slope of the Vøring Plateau is a case in point. The observations reveal considerable topographic steering and in particular a splitting of the currents at the topographic saddle point near 0E, 68N. This splitting is not reproduced by the thermal wind shear alone (Fig. 11a), but rather well by the simplified model (Fig. 11b). A second observed splitting of the western branch at Jan Mayen into a northward flow along the Mohn ridge and a southward flow along the Jan Mayen ridge also appears to imply non-zero bottom flows. The latter branch takes part in a general cyclonic circulation around the Norwegian basin.
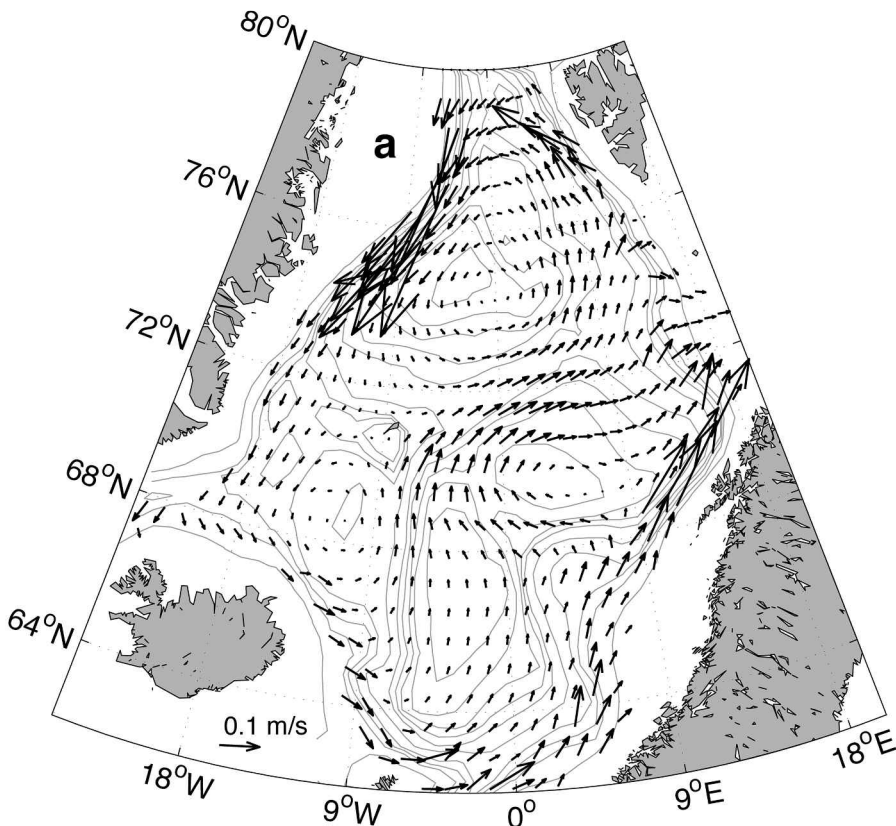
Figure 11. (a) Surface flow in the Nordic Seas given zero geostrophic velocity at the bottom. This field is calculated from the density field by integrating through the thermal wind balance from the bottom. (b) Modeled surface flow obtained by adding the observed thermal wind shear to the modeled bottom currents (Fig. 8).

The simplified model suggests the presence of an interesting feature on the northwestern slope of the Lofoten Basin (near 71N and 0E): The surface flow there is in opposite direction to the bottom flow, implying a considerable vertical shear. A good correspondence with observed surface currents indicates that this is a robust feature.

b. Arctic Ocean

Surface drifter data from the Arctic Ocean are nonexistent and we are again left with moored current observations for direct comparison. The modeled near-bottom geostrophic circulation in the Arctic Ocean is shown in Figure 12 together with near-bottom currents observed from moored instruments as reported by various investigators. The overall picture is in agreement with the conclusions drawn by Aagaard (1989) regarding the sub-surface circulation in the Arctic Ocean. These consist of the pronounced counter-
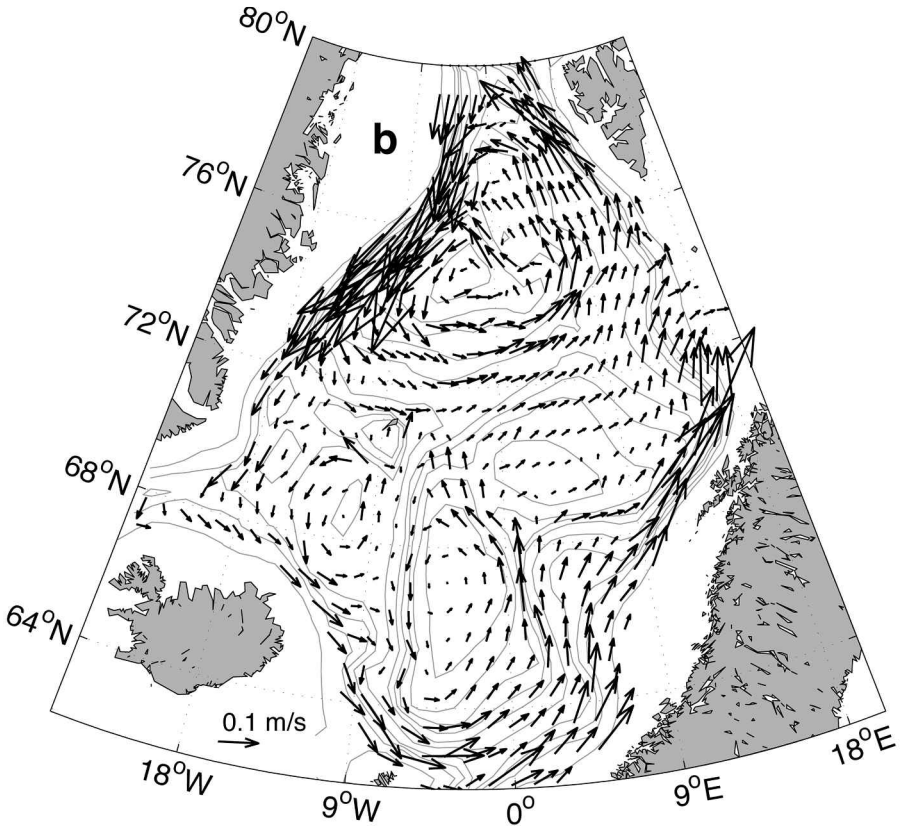
Figure 11. (Continued)

clockwise Arctic Circumpolar Boundary Current along the perimeter of the entire region and weaker flows within the individual sub basins.

In the interior of the Canadian Basin the modeled bottom flow is anticyclonic, in the opposite direction to the ACBC in this region. Citing current measurements from the continental slope north of Alaska and the results of Newton and Coachman (1974) and Aagaard (1984), Aagaard (1989) draws a picture of the sub-surface circulation in the Canadian Basin which is almost identical to our results (see his Fig. 11). Observations from the internal Beaufort Gyre are sparse. However, basing their analysis on a few direct current measurements, dynamic height calculations and water mass retention analysis, Newton and Coachman (1974) concluded that there is an anticyclonic circulation of Atlantic Water in the inner gyre coexisting with a narrow cyclonic boundary current along the continental slope. Generally, this circulation picture is in agreement with our model results, although the strong currents along the slope east of the Chuchi Plateau does not agree with the current measurements by Newton and Coachman (1974) shown in Figure 12.
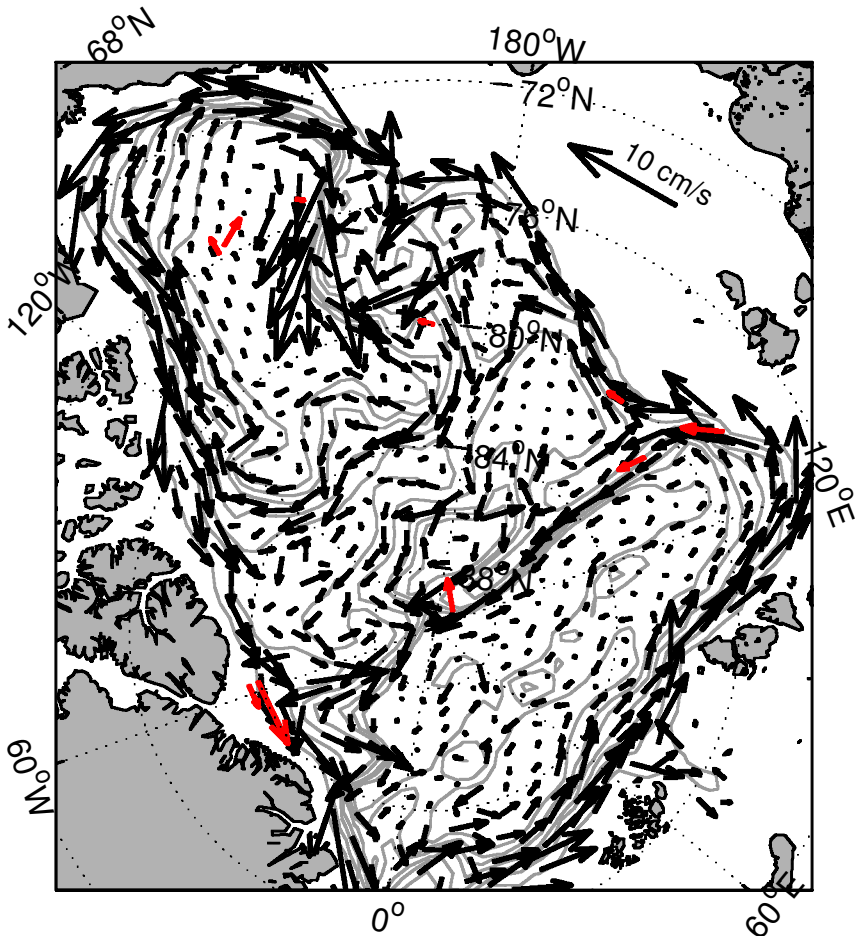
Figure 12. Modeled bottom geostrophic velocities (black arrows) and observed near bottom currents
    (red arrows) for the Arctic Ocean. The sources of the observed near bottom currents are Newton
    and Coachman (1974) (Canada Basin), Newton and Sotirin (1997) (Lincoln Sea), Aagaard (1981)
    (Lomonosov Ridge near the North Pole), Woodgate *et al.* (2001) (the three current meter moorings
    near 140W, 80N).

    The Eurasian Basin bottom flow is cyclonic from the outer rims, defined by the ACBC,
to its center. Woodgate et al. (2001) presented recent results of three current meter
moorings near 80N, 150E. The model predictions are in good agreement with their
findings: The ACBC splits in this region, into one branch following the continental slope
toward the Canadian Basin and another branch flowing toward the North Pole along the
Lomonosov Ridge. Near the North Pole there is a gap in the Lomonosov Ridge and the
model predicts a bottom flow into the Makarov Basin following the f/H contours. This flow

into the Makarov Basin might be a model artifact, as it strongly depends on a correct representation of the opening in the Lomonosov Ridge by the topographic dataset. A current meter on the slope of the Lomonosov Ridge (Aagaard, 1981) seems to confirm this flow, but whether the direction of this measured current is a result of local topography or the large scale circulation field is unknown. Finally, in the Lincoln Sea, where the Lomonosov Ridge runs into Greenland, bottom currents turn eastward and join the branch of the ACBC which has taken the long way around the Arctic. The comparison of modeled bottom flows from this region with direct observations reported by Newton and Sotirin (1997) is good.

4. Summary and discussion

We have presented a simplified model of the large-scale circulation within the Nordic Seas and Arctic Ocean. The model relies heavily on the fact that the f/H field forms closed contours over much of these high-latitude regions and on observational evidence that bottom currents are strong. Dynamically it is similar to a steady version of the model used by Isachsen *et al.* (2003) to look at time variability of the recirculating flow. The notable difference is that in the present model the depth-averaged currents need not follow isolines of f/H; bottom currents do, but currents higher up in the water column may turn according to observed horizontal density gradients. The model is thus a diagnostic one, designed for the purpose of examining possible lowest-order balances governing the dynamics of the large-scale flow in these regions.

The model solves for bottom geostrophic velocities, and these are "forced" by surface Ekman pumping derived from climatological wind stresses and by divergences due to meridional thermal wind transport relative to the bottom, these also extracted from climatologies. Bottom stress is the only mechanism included to dissipate energy. Scaling arguments show that the bottom geostrophic flow must then be nearly parallel to f/H contours. This is also supported by a number of observations (Aagaard, 1989; Fahrbach *et al.,* 2001; Newton and Sotirin, 1997; Orvik *et al.,* 2001; Woodgate *et al.,* 1999; Woodgate *et al.,* 2001). We thus write the total velocity only in terms of the along-contour component. For closed f/H contours, all the dynamics is contained within the simple expressions for the bottom velocities, (26) for a quadratic stress law and (28) for a linear stress law.

The modeled flow is sensitive to the quality of the applied forcing. By using the wind stress from NCEP/NCAR reanalysis as forcing on the sea surface, we are ignoring the effect of the sea ice cover. Steele *et al.* (1997) have shown that on an annual average the force balance of the sea ice motion is mainly between air drag, water drag and internal stress gradient. However, the water drag on the ice is mainly oppositely directed to the air drag, even if the internal stress gradients in the ice are not negligible. This means that the curl of the ice-water drag is distributed similarly to the curl of the air-ice drag, but the ice-water drag will have a smaller magnitude than the air-ice drag due to the effect of internal stress gradients in the ice. This is especially important in the areas north of

Greenland and the Canadian Archipelago where the air-ice drag seems to be mainly balanced by internal ice stress gradients (Steele *et al.,* 1997). Therefore, using wind stress from the NCEP/NCAR reanalysis project as forcing for the ocean circulation will generally lead to an overestimate of the magnitude of the wind stress curl acting on the ocean, especially in the coastal regions north of Greenland and the Canadian Archipelago. The wind forcing in the Nordic Seas, which is mainly ice free, will be less affected by this than in the Arctic Ocean. The main picture of strong forcing in the Nordic Seas and weaker forcing in the Arctic, which is clearly seen in Figure 3, may therefore be even more pronounced if the effect of sea ice is included.

The EWG Arctic Atlas is a gridded field with 50 km resolution, and therefore, narrow features like the Arctic Circumpolar Boundary Current are probably not very well resolved. The actual data which the EWG Arctic Atlas is based upon also have quite coarse resolution in the Arctic Ocean and along the eastern and northern coasts of Greenland. However, in the time-mean dynamics presented in this paper the forcing is integrated over areas enclosed by f/H contours. When integrating over large areas the narrow features not resolved by the hydrographic data is likely to play a minor role. We therefore believe that the hydrographic forcing is quite realistic. On open contours the solutions are given by data from current meters and does not depend on the hydrographic forcing derived from the EWG Arctic Atlas.

Neglected processes, like eddy-topography interactions and horizontal diffusion of momentum, doubtlessly also play important roles in the governing dynamics in the ocean. The eddy-topography rectification mechanism suggested by Holloway (1987, 1992) acts to drive mean cyclonic currents over topographic lows. In the eastern slope of the Chuchi Plateau our model predicts a strong eastward current while observations (Newton and Coachman, 1974) and high-resolution primitive equation simulations (Aksenov and Coward, 2001) suggests a weaker westward motion. This is an eddy rich area (D'Asaro, 1988; Muench *et al.,* 2000), and the possible failure by our simple model to reproduce currents here may very well be due to an ignored contribution from eddy-topography interaction. But there are other alternative explanations. Lateral momentum exchange (possibly also caused by eddies) between the cyclonic boundary current and the anticyclonic interior might also lead to a westward flow in this area. Also, the sea ice cover may act to weaken the anticyclonic forcing over the Canadian Basin. This would lead to a weaker anticyclonic gyre with resulting weaker eastward flow on the eastern slope of the Chuchi Plateau.

Considering its extreme simplicity, the model nonetheless produces results in surprising agreement with observations. What does it tell us? Essentially, the bottom velocity at any point on a closed f/H contour, as given by (26) or (28), is a product of two factors: (1) the integrated forcing within that contour divided by the length of the contour and (2) the local slope of the f/H field relative to the mean slope around the contour. For open f/H contours that extend into the North Atlantic, the mean strength and direction of the circulation are
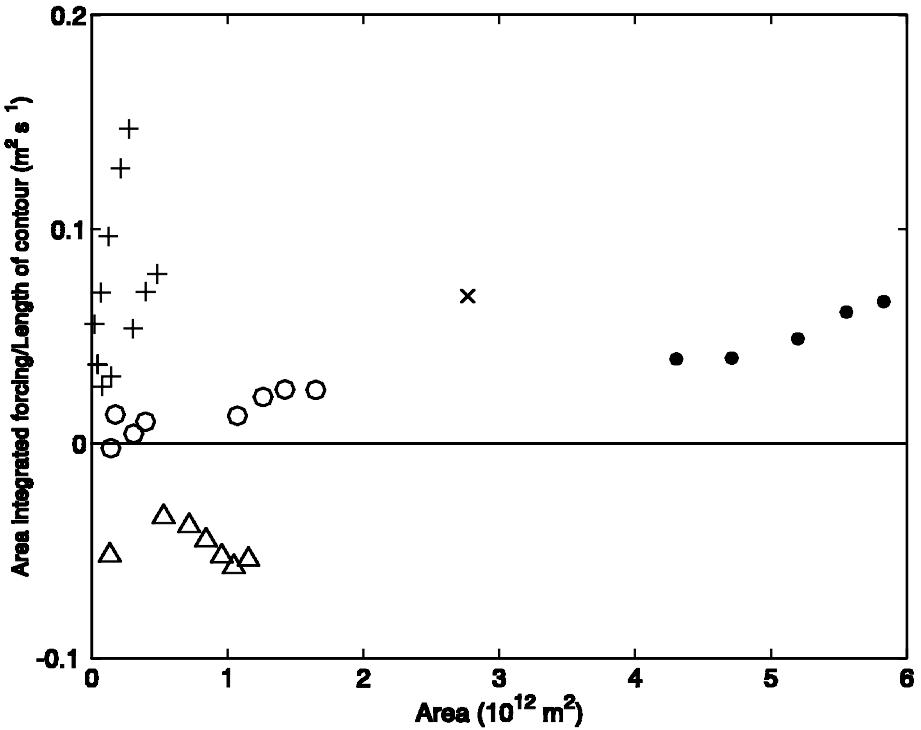
Figure 13. The total area-integrated forcing within f/H contours from various basins. Different regions are represented by symbols as follows: + Nordic Seas, ○ Eurasian Basin, △ Canadian Basin, × contours enclosing the Nordic Seas and the Eurasian Basin, ● contours enclosing the Nordic Seas and the whole Arctic Ocean.

estimated from direct current measurements, while the distribution of this flow along the contours is again a function of local f/H gradients.

The integrated forcing within closed contours is shown in Figure 13. It is this integrated forcing that determines the mean strength and direction of the flow along a contour. As can also be seen in Figure 3, the forcing is strong and cyclonic over the Nordic Seas, weak and cyclonic over the Eurasian Basin and anticyclonic over the Canadian Basin. The Arctic Circumpolar Boundary Current flows along the contours that encircle the entire domain north of the Greenland-Scotland Ridge, and the forcing on these contours depends on the integral over all the different basins. The end result turns out to be cyclonic bottom flow because the contribution from the strong cyclonic forcing in the Nordic Seas together with the weak cyclonic forcing in the Eurasian Basin dominates the anticyclonic forcing in the Canadian Basin. We therefore make the claim that the bottom cyclonic flow of the Arctic Circumpolar Boundary Current is largely forced from the Nordic Seas or, in the case of open f/H contours, from the world oceans south of the Greenland-Scotland Ridge. The inner anticyclonic motion in the Beaufort Gyre coexisting with a narrow cyclonic boundary
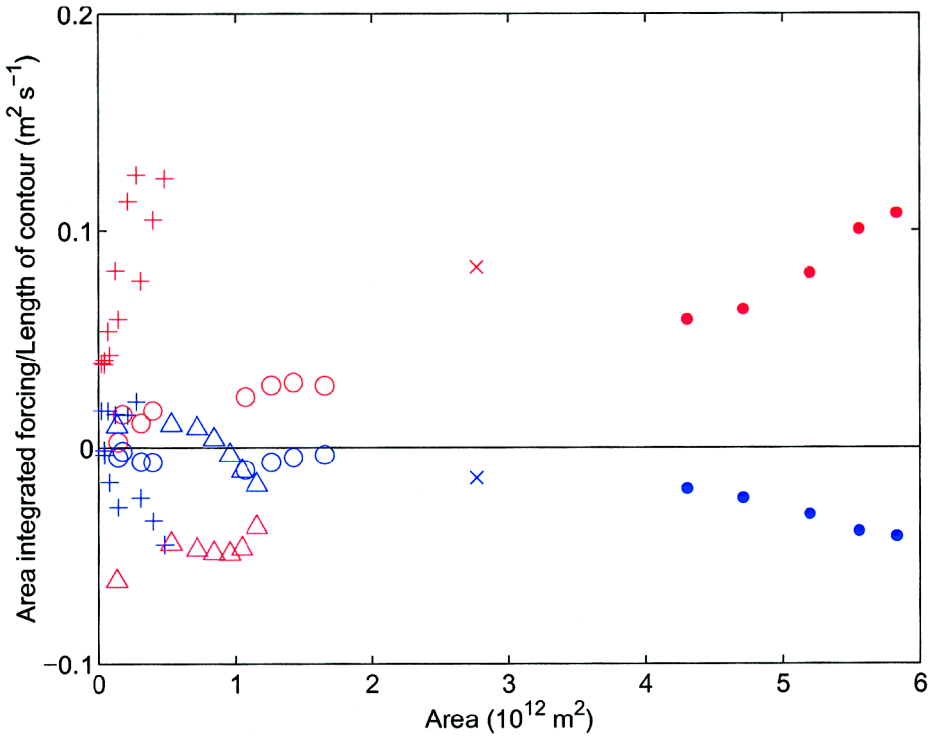
Figure 14. Contributions from the Ekman pumping (red) and the hydrographic forcing (blue) to the total area-integrated forcing within f/H contours from various basins. Different regions are represented by symbols as follows: + Nordic Seas, ○ Eurasian Basin, △ Canadian Basin, × contours enclosing the Nordic Seas and the Eurasian Basin, ● contours enclosing the Nordic Seas and the whole Arctic Ocean.

current along the rim of the basin is also explained from Figure 13. The circulation in the inner gyre is flowing along the f/H contours enclosing within the Canada basin where the forcing is anticyclonic, while the cyclonic boundary current is part of the remotely forced ACBC.

The organization of the f/H field is easily recognized in the flow: The flow accelerates as it enters regions where the f/H gradients sharpen and decelerates as it enters regions where the gradients weaken. An obvious example of this effect is the flow along the Norwegian continental slope from the Norwegian Basin and the Vøring plateau (low speeds), via the Lofoten Basin (large speeds), the Barents Sea Opening (low speeds) to the West Spitzbergen slope (large speeds).

Finally, we return to the integrated forcing, but now look at the relative contributions from wind and hydrography (Fig. 14). On just about every f/H contour the main contributor in driving the mean bottom flow is the surface Ekman pumping. The

divergence of the thermal wind shear is everywhere less important and, more noticeably, it is acting to drive the bottom flow in the opposite direction to that produced by the winds.

This is intriguing, and we wish to point out that these are not model results but a direct comparison of two independently generated data sets. The classic interpretation is that the density field has stored information about climatic surface stresses and is attempting to turn off the lower layer flow at long time scales (Anderson and Gill, 1975). Figure 14 suggests that the density field is attempting to turn off the lower layer flow without being able to do so completely. It is interesting to note that the attempted turn off of the bottom flow is clearly seen in the dataset which is integrated over areas enclosed by f/H contours (Fig. 14), while locally it does not seem to take place (compare Figs. 2a and 2b). This indicates that the thermal wind field in the Nordic Seas and Arctic Ocean may also depend on integrated potential vorticity balances within closed contours of f/H.

In the present diagnostic model the bottom geostrophic flow is forced by the part of the surface Ekman pumping which is not balanced by meridional flow in the upper layers. Possible mechanisms driving the bottom flow are interfacial stresses (Welander, 1968) or the eddy-induced rectifications suggested by either Holloway (1987, 1992) or Dewar (1998). However, Welander's results do not agree with the strong bottom currents observed in the Arctic, and it also seems worth noting that the eddy parameterizations used by Holloway and Dewar tend to drive the flow in the opposite sense to what is observed in the interior of the Canadian Basin. Instead, we interpret the success of the present diagnostic model as an indication that the potential vorticity input by surface winds is efficiently transmitted to the bottom. We close by reminding ourselves that both Welander's and Dewar's models were adiabatic. In high latitude oceans, non-adiabatic effects should be considered. Diapycnal mass fluxes, set up by buoyancy loss at the sea surface, may very well act to transfer potential vorticity from the surface to the bottom.

APPENDIX A

Is $\partial \psi_b / \partial q$ constant on an f/H contour?

The velocity across q contours is important to balance the depth-integrated vorticity equation (16) locally. Therefore, there will be gradients in ψ_b and $\partial \psi_b / \partial q$ along the q contours. Although these gradients are much smaller than the gradients directed across the q contours they might lead to significant changes of ψ_b and $\partial \psi_b / \partial q$ if the length scales along the q contours are much larger than the length scales across the contours. The ratio of the two velocity components in (22) scale as:

$$\frac{U_\perp}{U_\parallel} \approx \frac{\Delta \psi_\parallel}{\Delta \psi_\perp} \frac{L_\perp}{L_\parallel}, \tag{30}$$

where $\Delta\psi_\perp$ is the difference in ψ_b over a distance $L_\perp$ across the q contours, while $\Delta\psi_\parallel$ is the difference in ψ_b over a distance $L_\parallel$ along the q contours. For $\Delta\psi_\parallel$ to be as large as $\Delta\psi_\perp$, $U_\perp$ must vary with length scale $L_\parallel$ along the contours such that

$$\frac{L_\perp}{L_\parallel} \approx \frac{U_\perp}{U_\parallel} \approx \frac{C_D U}{f L_\perp |\nabla H|}, \tag{31}$$

where again the term on the right hand side is taken from (21).

From Figures 1 and 4 we see that the contours enclosing the whole domain of the Nordic Seas and Arctic Ocean have a topographic slope mainly of order larger than 10^{-2}. The Arctic Circumpolar Boundary Current, which is flowing along these contours, have a width roughly equal to the width of the continental slope, about 100 km. For a bottom flow of order 10^{-1} m s^{-1}, the ratio of the length scales in (31) becomes 10^{-3}. According to this we need a length scale ($L_\parallel$) of order 10^5 km to change $\partial\psi_b/\partial q$ significantly. The length of the contours is an order of magnitude smaller than this, suggesting that treating $\partial\psi_b/\partial q$ as a function of q is a reasonable assumption for the longest contours.

Next, for the interior sub-basins where the topographic slope is near 10^{-3}, the ratio of the length scales in (31) is about 10^{-2} for the same values of U and $L_\perp$. For these regions the width of the currents are mostly higher than 100 km, suggesting that the ratio of the length scales may be even smaller. Thus, a length scale larger than 10^4 km is needed to change $\partial\psi_b/\partial q$ significantly. As it turns out, the length of these contours within areas of topographic slope near 10^{-3} is again considerably shorter than this. In summary, it appears that ψ_b, and hence $\partial\psi_b/\partial q$, can be treated as a function of q for the entire domain.

APPENDIX B

Dynamics of an idealized basin

To investigate the dynamics in a basin with closed f/H contours and steep topography more closely, we solve the depth integrated vorticity equation (16) for an idealized basin. The topography of the idealized basin is given by:

$$H = -H_0 e^{[-(r^2/L^2)]} - H_1 \tag{32}$$

where r is the radius from the center of the gyre given by $r^2 = (x - x_0)^2 + (y - y_0)^2$, $H_0 = 3700$ m, $H_1 = 300$ m and $L = 6 \cdot 10^5$ m (Fig. 15a). x_0 and y_0 represent the point in the center of the domain. The forcing (F), representing the right hand side of (16), is given by:

$$F = F_0 \left(\frac{x}{x_0}\right)^2 \tag{33}$$

The forcing with $F_0 = 5 \cdot 10^{-7}$, is shown in Figure 15b.

The coriolis parameter f is constant ($f = 1.2 \cdot 10^{-4}$ s^{-1}), and the bottom stress is
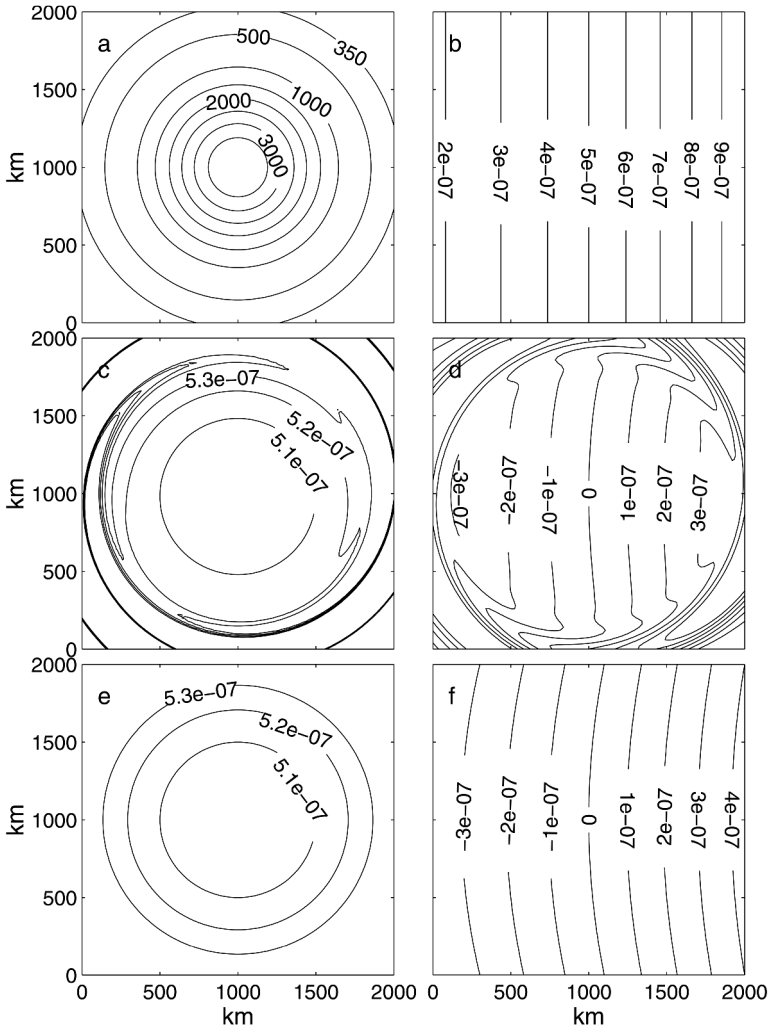
Figure 15. Closed f/H flow in an idealized basin. (a) Topography of the idealized basin, (b) forcing of the idealized basin, (c) the friction term $((R/f)\nabla \times \mathbf{v}_b)$ as calculated by the numerical model, (d) the topographic term $(-\mathbf{v}_b \cdot \nabla H)$ as calculated by the numerical model, (e) the friction term as calculated by the analytical model (39), and (f) the topographic term as calculated by the analytical model (40). All units are given in m s^{-1} except for the topography which is given in meters.

parametrized using a linear friction law (19), with $R = 10^{-4}$ m s^{-1}. With these simplifications (16) becomes:

$$-\mathbf{v}_b \cdot \nabla H + \frac{R}{f}\nabla \times \mathbf{v}_b = F \qquad (34)$$

By the use of the geostrophic approximation for the bottom velocity (10), (34) may be written as:

$$-\frac{1}{\rho_0 f} J(\psi_b, H) + \frac{R}{\rho_0 f^2} \nabla^2 \psi_b = F \tag{35}$$

Here J is the Jacobian defined as: $J(a, b) = (\partial a/\partial x)(\partial b/\partial y) - (\partial a/\partial y)(\partial b/\partial x)$.

We solve (35) numerically in a rectangular domain by approximating all derivatives with a centered finite difference scheme and no-slip boundary conditions at the walls. The resulting set of linear equations are solved by gaussian elimination. The numerical model was set up on a rectangular domain 5000*5000 km with a resolution of 20 km. The frictional parameter R was increased towards the walls for $r > 1500$ km (which is well outside the area of interest) to avoid noisy behavior of the model near the boundaries. The contributions from the different terms in the vorticity equation (34 or 35) are shown in Figure 15c and 15d, and the computed bottom velocity field is shown in Figure 16a.

When the component of the bottom velocity along the f/H contours is much larger than the component perpendicular to the contours, the bottom velocity may be calculated from (28), which in the case of constant f and forcing given by F becomes:

$$v_b = \frac{f}{R} \frac{\displaystyle\iint_A F dA}{\displaystyle\oint_C |\nabla H| dl} |\nabla H| t \tag{36}$$

As before t is the unit tangent vector to the isobaths in a counter-clockwise direction. With the given forcing and topography we can find an analytical expression for the area-integral of the forcing:

$$\iint_A F dA = \pi r^2 F_0 \left(\frac{r^2}{4x_0^2} + 1 \right) \tag{37}$$

Using this equation together with (32) and (36) v_b may be expressed as:

$$v_b = \frac{f F_0}{8 R x_0^2} (r^3 + 4x_0^2 r) t \tag{38}$$

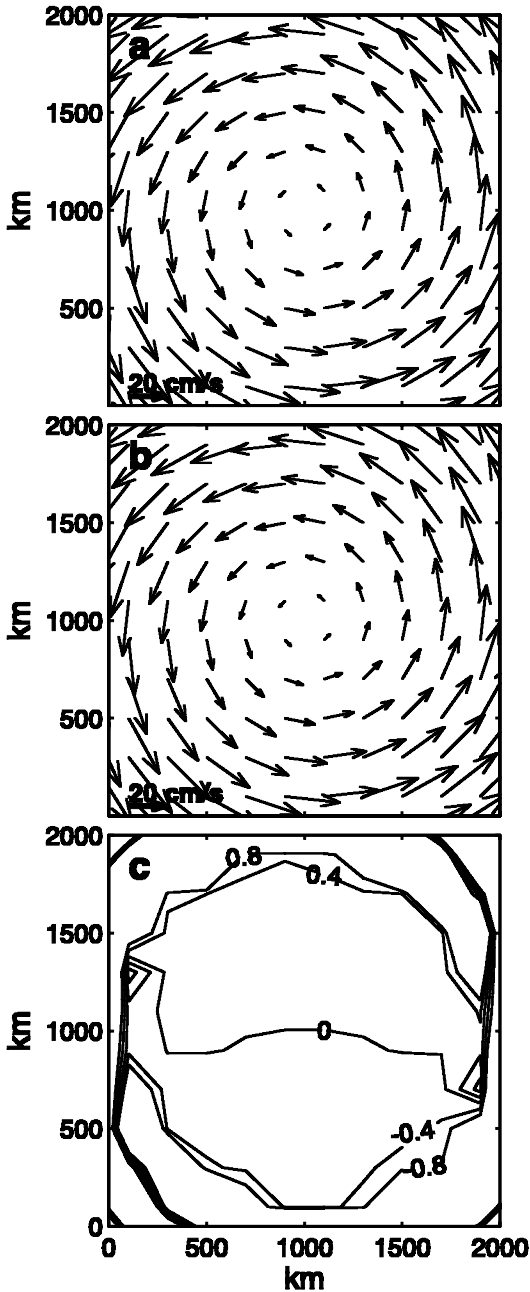The bottom friction term may now be calculated from (38):

Figure 16. Results of the idealized basin model. (a) The velocity field calculated by the numerical model. (b) The velocity field calculated by the analytical model. (c) The difference between the velocity fields calculated by the numerical and analytical model in percent.

$$\nabla \times \frac{\boldsymbol{\tau}_b}{\rho_0 f} = \frac{R}{f} \nabla \times \boldsymbol{v}_b = F_0 \left(\frac{r^2}{2x_0^2} + 1 \right) \tag{39}$$

It is easily verified that the area integral of the bottom friction term, given by (39) equals the area-integral of the forcing (F), which is in agreement with (17).

The topographic term, which is the first term in (34), may now be found by the use of (34), (38) and (39):

$$-\boldsymbol{v}_b \cdot \nabla H = F - \frac{R}{f} \nabla \times \boldsymbol{v}_b = F_0 \left(\frac{x^2}{x_0^2} - \frac{r^2}{2x_0^2} - 1 \right) \tag{40}$$

The analytical expressions for the friction term and the topographic term given by (39) and (40) is shown in Figure 15e and 15f, where they can be compared to the same terms in the numerical model. The analytical velocity field given by (38) is also shown in Figure 16b, and the difference between this expression for $\boldsymbol{v}_b$ and the velocity in the numerical model is less than 1 percent (Fig. 16c).

Figure 15 illustrates an important element in the dynamics of basins with closed f/H contours and steep topography. The shape of the friction term is fully controlled by the bottom topography, because the bottom geostrophic velocity has to follow the depth contours. This means that the friction term is only able to balance the integrated balances, represented by (17), while it is not able to balance the east west asymmetry in the forcing shown in Figure 15b. The bottom vortex stretching, represented by the term $-\boldsymbol{v}_b \cdot \nabla H$ is not able to balance the area-integrated forcing since the mean of this term over an area enclosed by an f/H contour is always zero. However, the bottom vortex stretching is the only term that is able to balance the east west asymmetry in the forcing, making sure that the depth integrated vorticity equation (equation 16 or 34 in the idealized case) is balanced locally.

REFERENCES

Aagaard, K. 1970. Wind-driven transports in the Greenland and Norwegian seas. Deep-Sea Res., *17,* 281–291.

——1981. On the deep circulation in the Arctic Ocean. Deep-Sea Res., *28A,* 251–268.

——1984. The Beaufort undercurrent, *in* The Alaskan Beaufort Sea, P. W. Barnes, D. M. Schell, and E. Reimnitz, eds., Orlando: Academic Press, 47–71.

——1989. A synthesis of the Arctic Ocean circulation. Rapp. P.-v. Reun. Cons. int. Explor. Mer, *188,* 11–22.

Aksenov, Y. and A. C. Coward. 2001. The Arctic Ocean circulation as simulated in a very high-resolution global ocean model. Annals of Glaciology, *33,* 567–576.

Anderson, D. L. T. and A. E. Gill. 1975. Spin-up of a stratified ocean, with application to upwelling. Deep-Sea Res., *22,* 583–596.

Bogden, P. S., R. E. Davis and R. Salmon. 1993. The North Atlantic circulation: Combining simplified dynamics with hydrographic data. J. Mar. Res., *51,* 1–52.

Conkright, M., S. Levitus, T. O'Brien, T. Boyer, J. Antonov and C. Stephens. 1998. World Ocean Atlas 1998 CD-ROM Data Set Documentation. Tech. Rep. 15, NODC Internal Report, National Ocean Data Center, Silver Spring, MD.

D'Asaro, E. A. 1988. Observations of small eddies in the Beaufort Sea. J. Geophys. Res., *93*(C6), 6669–6684.

de Miranda, A. P., B. Barnier and W. K. Dewar. 1999. On the dynamics of the Zapiola Anticyclone. J. Geophys. Res., *104*(C9), 21137–21149.

Dewar, W. K. 1998. Topography and barotropic transport control by bottom friction. J. Mar. Res., *56,* 295–328.

Fahrbach, E., J. Meincke, S. Østerhus, G. Rohardt, U. Schauer, V. Tverberg, J. Verduin and R. A. Woodgate. 2001. Direct measurements of heat and mass transports through Fram Strait. Polar Research, The Sverdrup Volume, 217–224.

Haidvogel, D. B. and A. Beckmann. 1999. Numerical Ocean Circulation Modelling, Volume 2 of Series of Environmental Science and Management. Imperial College Press.

Hasselmann, K. 1982. An ocean model for climate variability studies. Progr. Oceanogr., *11,* 69–92.

Helland-Hansen, B. and F. Nansen. 1909. The Norwegian Sea—its physical oceanography based upon the Norwegian researches 1900–1904, *in* Report on Norwegian Fishery and Marine Investigations, II, Johan Hjort, ed., The Royal Department of Trade, Navigation and Industries, 1–360.

Holloway, G. 1987. Systematic forcing of large scale geophysical flows by eddy-topography interaction. J. Fluid Mech., *184,* 463–476.

——1992. Representing topographic stress for large-scale ocean models. J. Phys. Oceanogr., *22,* 1033–1046.

Isachsen, P. E., J. H. LaCasce, C. Mauritzen and S. Häkkinen. 2003. Wind-driven variability of the large-scale recirculation flow field in the Nordic Seas and Arctic Ocean. J. Phys. Oceanogr., (submitted).

Jakobsen, P. K., M. H. Ribergaard, D. Quadfasel, T. Schmith and C. Hughes. 2003. The near surface circulation in the Northern North Atlantic as inferred from Lagrangian drifters: variability from mesoscale to interannual. J. Geophys. Res. (in press).

Jónsson, S. 1991. Seasonal and interannual variability of wind stress curl over the Nordic Seas. J. Geophys. Res., *96*(C2), 2649–2659.

Kalnay, E., M. Kanamitsu, R. Kistler, W. Collins, D. Deaven, L. Gandin, M. Iredell, S. Saha, G. White, J. Woollen, Y. Zhu, M. Chelliah, W. Ebisuzaki, W. Higgins, J. Janowiak, K. C. Mo, C. Ropelewski, J. Wang, R. R. A. Leetmaa and R. J. D. Joseph. 1996. The NCEP/NCAR 40-year reanalysis project, Bull. Amer. Meteorol. Soc., *77*(3), 437–471.

Legutke, S. 1991. A numerical investigation of the circulation in the Greenland and Norwegian Seas. J. Phys. Oceanogr., *21,* 118–148.

Muench, R. D., J. T. Gunn, T. E. Whitledge, P. Schlosser and W. Smethie. 2000. An Arctic Ocean cold core eddy. J. Geophys. Res., *105*(C10), 23997–24006.

National Geophysical Data Center. 1995. Terrainbase. CD-ROM.

Nazarenko, L., G. Holloway and N. Tausnev. 1998. Dynamics of transport of "Atlantic signature" in the Arctic Ocean. J. Geophys. Res., *103*(C13), 31003–31015.

Nazarenko, L. and N. Tausnev. 2001. Modeling of the Beaufort ice-ocean climatology change. Annals of Glaciology, *33,* 560–566.

Newton, J. L. and L. K. Coachman. 1974. Atlantic water circulation in the Canada Basin. Arctic, *27,* 297–303.

Newton, J. L. and B. J. Sotirin. 1997. Boundary undercurrent and water mass changes in the Lincoln Sea. J. Geophys. Res., *102*(C2), 3393–3403.

Orvik, K. A. and P. Niiler. 2002. Major pathways of Atlantic water in the northern North Atlantic and Nordic Seas toward Arctic. Geophys. Res. Lett., *29*(19), 2–1 to 2–4. doi:10.1029/2002GL015002.

Orvik, K. A., Ø. Skagseth and M. Mork. 2001. Atlantic inflow to the Nordic Seas: current structure

and volume fluxes from moored current meters, VM-ADCP and SeaSoar-CTD observations, 1995–1999. Deep-Sea Res. I, *48*(4), 937–957.

Polyakov, I. 2001. An eddy parameterization based on maximum entropy production with application to modelling of the Arctic Ocean circulation. J. Phys. Oceanogr., *31,* 2255–2270.

Poulain, P. M., A. Warn-Varnas and P. P. Niiler. 1996. Near-surface circulation of the Nordic seas as measured by Lagrangian drifters. J. Geophys. Res., *101*(C8), 18237–18258.

Rhines, P. B. and W. R. Young. 1982. A theory of wind-driven circulation. I. Mid-ocean gyres. J. Mar. Res., *40,* 559–596.

Rudels, B., H. J. Friedrich and D. Quadfasel. 1999. The Arctic circumpolar boundary current. Deep-Sea Res. II, *46,* 1023–1062.

Saunders, P. M. and B. A. King. 1995. Bottom currents derived from a shipborne ADCP on the WOCE cruise A11 in the South Atlantic. J. Phys. Oceanogr., *25,* 329–347.

Steele, M., J. Zhang, D. Rothrock and H. Stern. 1997. The force balance of sea ice in a numerical model of the Arctic Ocean. J. Geophys. Res., *102*(C9), 21061–21079.

Timokhov, L. and F. Tanis, eds. 1997. Arctic Climatology Project. 1997. Environmental Working Group Joint U.S.-Russian Atlas of the Arctic Ocean—Winter Period. Ann Arbor, MI: Environmental Research Institute of Michigan in association with the National Snow and Ice Data Center. CD-ROM.

——1998. Arctic Climatology Project. 1998. Environmental Working Group Joint U.S.-Russian Atlas of the Arctic Ocean—Summer Period. Ann Arbor, MI: Environmental Research Institute of Michigan in association with the National Snow and Ice Data Center. CD-ROM.

Welander, P. 1968. Wind-driven circulation in one- and two-layer oceans of variable depth. Tellus, *20,* 1–15.

Woodgate, R. A., K. Aagaard, R. D. Muench, J. Gunn, G. Bjørk, B. Rudels, A. T. Roach and U. Schauer. 2001. The Arctic Ocean boundary current along the eurasian slope and the adjacent Lomonosov Ridge: Water mass properties, transports and transformations from moored instruments. Deep-Sea Res. I, *48,* 1757–1792.

Woodgate, R. A., E. Fahrbach and G. Rohardt. 1999. Structure and transports of the East Greenland Current at 75N from moored current meters. J. Geophys. Res., *104*(C8), 18059–18072.